Quantum processes in short and intensive electromagnetic fields

Alexander I. Titov[a], Burkhard Kämpfer[b,c], Atsushi Hosaka[d,e], and Hideaki Takabe[f]

[a] *Bogoliubov Laboratory of Theoretical Physics, JINR, Dubna 141980, Russia*

[b] *Helmholtz-Zentrum Dresden-Rossendorf, 01314 Dresden, Germany*

[c] *Institut für Theoretische Physik, TU Dresden, 01062 Dresden, Germany*

[d] *RCNP, 10-1 Mihogaoka Ibaraki, 567-0047 Osaka, Japan*

[e] *J-PARC Branch, KEK, Tokai, Ibaraki, 319-1106, Japan*

[f] *ILE, Yamada-oka, Suita, Osaka 565-0871, Japan*

Abstract

This work provides an overview of our recent results in studying two most important and widely discussed quantum processes: electron-positron pairs production off a probe photon propagating through a polarized short-pulsed electromagnetic (e.g. laser) wave field or generalized Breit-Wheeler process, and a single a photon emission off an electron interacting with the laser pules, so-called non-linear Compton scattering. We show that the probabilities of particle production in both processes are determined by interplay of two dynamical effects, where the first one is related to the shape and duration of the pulse and the second one is non-linear dynamics of the interaction of charged fermions with a strong electromagnetic field. We elaborate suitable expressions for the production probabilities and cross sections, convenient for studying evolution of the plasma in presence of strong electromagnetic fields

PACS numbers: 12.20.Ds, 13.40.-f, 23.20.Nx

Keywords: Non-linear dynamics, multi-photon effects, sub-threshold processes

I. INTRODUCTION

The rapidly progressing laser technology [1] offers unprecedented opportunities for investigations of quantum systems with intense laser beams [2]. A laser intensity I_L of $\sim 2\times10^{22}$ W/cm^2 has been already achieved [3]. Intensities of the order of $I_L \sim 10^{23}...10^{25}$ W/cm^2 are envisaged in near future, e.g. at the CLF [4], ELI [5], HiPER [6]. Further facilities are in planning on construction stage, e.g. PEARL laser facility [7] at Sarov/Nizhny Novgorod, Russia. The high intensities are provided in short pulses on a femtosecond pulse duration level [2, 8, 9], with only a few oscillations of the electromagnetic (e.m.) field or even subcycle pulses. In order to achieve such high intensities in the focal spot of the laser beam a crucial technique is required. (The tight connection of high intensity and short pulse duration is further emphasized in [10]. The attosecond regime will become accessible at shorter wavelengths [11, 12]).

Quantum processes occurring in the interactions of charge fermions in very (infinitely) long e.m. pulse were investigated in detail in the pioneering works of Reiss [13, 14] as well as Narozhny, Nikishov and Ritus [15, 16] and some other papers (see for example [17]). We call the such approaches as an infinite pulse approximation (IPA) since it refers to a stationary scattering process. Many simple and clear expressions for the production probabilities and cross sections have been obtain within IPA. It was shown that the charged fermion (electron, for instance) can interact with $n \geq 1$ photon simultaneously (n is an integer number), and cases with $n > 1$ correspond to the subthreshold, multi-photon events. However, since the new laser generation is expected to operate with the finite (short, and ultra-short) pulses, the question naturally arises whether predictions of IPA are valid for the finite pulses or not.

Indeed, recently it was shown that for the photon production off an electron interacting with short laser pulse (Compton scattering) in [10, 18–24], and for e^+e^- pair production off a probe photon interacting with short e.m. pulses (Breit-Wheeler process) in [25–29] the finite pulse shape and the pulse duration become important. That means the treatment of the intense and short laser field as an infinitely long wave train is no longer adequate. The theory must operate with essentially finite pulse. We call such approaches as a finite pulse approximation (FPA). Formation of positrons from cascade processes in a photon-electron-positron plasma [30, 31] generated by photon-laser [32], electron-laser [33, 34] or laser-laser interactions [35] (see [36, 37] for surveys) is an important problem in laser physics. The

evaluation of corresponding transport equations needs as an input the probabilities/cross sections for the production energetic photons (e.g., in the non-linear Compton scattering) and direct emission of e^+e^- pairs (e.g., in the non-linear Breit-Wheeler process).

Consider first the non-linear Breit-Wheeler process. Corresponding linear Breit-Wheeler e^+e^- pair production $\gamma' + \gamma \to e^+ + e^-$ [38] refers to a perturbative QED reaction; the generalization to the multi-photon process $\gamma' + n\gamma \to e^+ + e^-$ (nonlinear Breit-Wheeler process) in IPA were done in [13, 16, 17]. Attributing theses processes to colliding null fields one can imagine another aspect. In the anti-node of suitably counter propagating e.m. waves an oscillating purely electric field can give rise to the dynamical Schwinger effect [39]; in the low-frequency limit one recovers the famous Schwinger effect [40] awaiting still its experimental verification. These kinds of pair creation processes are related to highly non-perturbative effects [41, 42]. Once pair production is seeded in very intense fields further avalanche like particle production can set in which then could screen the original field or even limit the attainable field strength [30]. One can relate the Breit-Wheeler process to the absorptive part of the probe-photon correlator in an external e.m. field; in our case the latter being a null field too. Later, we focus on colliding null fields in the multi-photon regime and consider the generalized Breit-Wheeler effect for short pulses of e.m. wave fields ranging from weak to high intensities. Phrased differently we analyze e^+e^- pair production by a probe photon γ' traversing a coherent e.m. (i.e. laser) field. We employ the four-potential of a circularly polarized laser field in the axial gauge $A^\mu = (0,\, \mathbf{A}(\phi))$ with

$$\mathbf{A}(\phi) = f(\phi)\left(\mathbf{a}_1 \cos(\phi + \tilde{\phi}) + \mathbf{a}_2 \sin(\phi + \tilde{\phi})\right) \ , \tag{1}$$

where $\phi = k \cdot x$ is invariant phase with four-wave vector $k = (\omega, \mathbf{k})$, obeying the null field property $k^2 = k \cdot k = 0$ (a dot between four-vectors indicates the Lorentz scalar product) implying $\omega = |\mathbf{k}|$, $\mathbf{a}_{(1,2)} \equiv \mathbf{a}_{(x,y)}$; $|\mathbf{a}_x|^2 = |\mathbf{a}_y|^2 = a^2$, $\mathbf{a}_x\mathbf{a}_y = 0$; transversality means $\mathbf{k}\mathbf{a}_{x,y} = 0$ in the present gauge. The envelope function $f(\phi)$ with $\lim\limits_{\phi\to\pm\infty} f(\phi) = 0$ (FPA) accounts for the finite pulse length. (IPA would mean $f(\phi) = 1$). To define the pulse duration one can use the number N of cycles in a pulse, $N = \Delta/\pi = \frac{1}{2}\tau\omega$, where the dimensionless quantity Δ or the duration of the pulse τ are further useful measures. The carrier envelope phase $\tilde{\phi}$ is particularly important if it is varied in a range comparable with the pulse duration Δ. In IPA it is anyhow irrelevant; in FPA with $\tilde{\phi} \simeq \Delta$ the cross section of the photon emission would be determined by an involved interplay of the carrier phase, the pulse duration and pulse

shape as well as the intensity of e.m. field as emphasized, e.g., in [43]) (see also [28, 44]). In the beginning, we drop the carrier phase, thus assuming $\tilde{\phi} \ll \Delta$, and concentrate on the dependence of the cross sections on the parameters responsible essentially for multi-photon effects. Impact of $\tilde{\phi}$ on the differential production rate is discussed in Sects. 3. 7 and 4. 4. In present consideration we drop effect of the pulse focusing which, however, is more relevant for longer pulses [45] than those covered in the present review where we consider pulses with number of oscillations less than ten.

The interaction of an electron with e.m. field is characterized by the dimensionless field intensity ξ^2. For simplicity, let us consider case of generalized Compton scattering where the variable ξ^2 can be determined through the average value of the manifestly covariant variable $\eta = T^{\mu\nu} p_\mu p_\nu/(p\cdot k)^2$ [46] (cf. also [15]), where p is the four-momentum of a target electron, and $T^{\mu\nu}$ is the e.m. stress-energy tensor $T^{\mu\nu} = g_{\alpha\beta}F^{\mu\alpha}F^{\beta\nu} + \frac{1}{4}g^{\mu\nu}F_{\alpha\beta}F^{\alpha\beta}$ where $F_{\mu\nu} = \partial_\mu A_\nu - \partial_\nu A_\mu$ stands for the e.m. field strength tensor. In the charge's rest frame $\eta = T^{00}/\omega^2$, where the stress-energy tensor T^{00} is equal to the energy density of the e.m. field or to the pulse intensity I_L. In IPA, the quantity ξ^2 is determined by

$$\xi^2 = \frac{e^2}{m^2}\frac{1}{\tau_{IPA}}\int\limits_{-\tau_{IPA}/2}^{\tau_{IPA}/2} dt\ \eta = \frac{e^2}{m^2\omega^2}\frac{1}{2\pi}\int\limits_{-\pi}^{\pi} d\phi\ I_L = \frac{e^2 a^2}{m^2}\ , \tag{2}$$

where the averaging interval is set equal to the duration of one cycle, $\tau_{IPA} = 2\pi/\omega$ (we use natural units with $c = \hbar = 1$, $e^2/4\pi = \alpha \approx 1/137.036$). The generalization to a finite pulse may be done in a straightforward manner:

$$\xi^2_{FPA} = \frac{e^2}{m^2}\frac{1}{\tau_{FPA}}\int\limits_{-\infty}^{\infty} dt\ \eta = \frac{e^2}{m^2\omega^2}\frac{1}{2\pi N}\int\limits_{-\infty}^{\infty} d\phi\ I_L\ . \tag{3}$$

Now, the interval τ_{FPA} is determined by the number N of oscillations in a pulse as $2\pi N/\omega$. That is, the quantity ξ^2, which defines the production probability and the cross section, can be expressed through the averaged value of the intensity of a finite laser pulse

$$\xi^2 = \xi^2_{FPA}\frac{N}{N_0}\ , \tag{4}$$

or

$$\begin{aligned}\xi^2 = \frac{N}{N_0}\frac{e^2}{\omega^2 m^2}\langle I_L\rangle\ &\simeq\ \frac{N}{N_0}\frac{5.62\cdot 10^{-19}}{\omega^2[\mathrm{eV}^2]}\langle I_L\rangle\left[\frac{\mathrm{W}}{\mathrm{cm}^2}\right] \\ &\simeq\ \frac{N}{N_0}\,3.66\cdot 10^{-19}\lambda^2[\mu\mathrm{m}^2]\langle I_L\rangle\left[\frac{\mathrm{W}}{\mathrm{cm}^2}\right]\ ,\end{aligned} \tag{5}$$

where $\lambda = 2\pi/\omega$ is wave lenght of the background field and $N_0 \langle I_L \rangle = (\omega/2\pi) \int_{-\infty}^{\infty} dt\, I_L$. Hence, the normalization factor N_0 is determined as

$$N_0 = \frac{1}{2\pi} \int\limits_{-\infty}^{\infty} d\phi \, (f^2(\phi) + f'^2(\phi)) \tag{6}$$

and has a meaning of renormalized factor for the photon flux in the case of finite pulse. The factor N_0 is described in some detail below in Sect. II. In fact, for the realistic envelope functions $N_0 \simeq N$ and, therefore, $\xi^2 \simeq \xi^2_{FPA}$. The generalization to the Breit-Wheeler process can be done strightforward by substitution $p \to k'$ and utilizing the center of mass system.

For completeness, in Fig. 1 we exhibit explicit dependence of ξ^2 on I_L for different wave lengths for $N = N_0$. Dashed, solid and dot-dashed curves are for $\lambda = 40$, 0.8, and 0.01 μm,

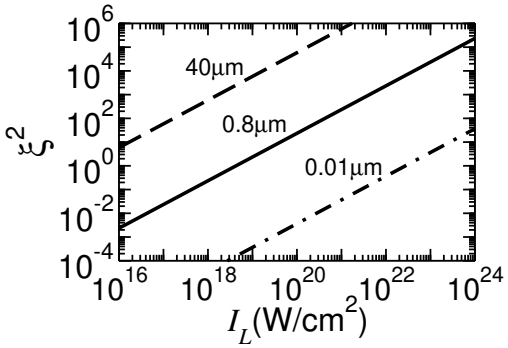

FIG. 1: Reduced field intensity ξ^2 as a function of averaged pulse intensity I_L for different wave lengths. Dashed, solid and dot-dashed curves are for $\lambda = 40$, 0.8, and 0.01 μm, respectively.

respectively, which correspond to the infrared, optic, and X-ray scales.

A second relevant dimensionless variable characterizing both null fields is

$$\zeta = \frac{s_{\rm thr}}{s}, \tag{7}$$

where $s_{\rm thr} = 4m^2$ and $s = 2\omega\omega'(1 - \cos\Theta_{\mathbf{k}\mathbf{k}'})$ (for head-on collision geometry, $\Theta_{\mathbf{k}\mathbf{k}'} = \pi$); ω, ω' and $\mathbf{k}, \mathbf{k}'$ are the frequencies and three-wave vectors of the laser field and the probe photon, respectively. The variable $s_{\rm thr}$ is the square of the initial energy at the threshold therefore, the variable ζ is a pure kinematic quantity with the meaning that for $\zeta > 1$ the linear Breit-Wheeler process $\gamma' + \gamma \to e^+ + e^-$ is sub-threshold, i.e. kinematically forbidden. However, multi-photon effects enable the non-linear process $\gamma' + n\gamma \to e^+ + e^-$ even for $\zeta > 1$

which we refer as sub-threshold pair production. The non-linear Breit-Wheeler process has been experimentally verified in the experiment E-144 at SLAC [47]. There, the minimum number of photons involved in one e^+e^- event can be estimated by the integer part of $\zeta(1+\xi^2)$, i.e., five. To arrive at such an estimate we recall that the reduced strength ξ is related to the laser intensity I_L via Eq. (5), and therefore, at $\omega' = 29$ GeV, $\omega = 2.35$ eV, and at peak focused laser intensity of $1.3 \times 10^{18}\,\mathrm{W/cm^2}$, one gets $\xi = 0.36$ and $\zeta = 3.83$. The laser pulses contained about thousand cycles in a shot, allowing to neglect the details of the pulse shape and duration.

Some important difference between IPA and FPA is that in the first case the variable $n = 1, 2, \cdots$ is integer, it refers to the contribution of the individual harmonics. The value $n\omega$ is related to the energy of the background field involved into considered quantum process. Obviously, this value is a multiple of ω. In FPA, the basic subprocess operate with l *background photons*, where l is a continuous variable. The quantity $l\omega$ can be considered as the energy partition of the laser beam involved into considered process, and it is not a multiple ω. Mindful of this fact, without loss of generality, we denote the processes with $l > 1$ as a generalized multi-photon processes, remembering that l is a continuous quantity.

The Compton process is considered below as a spontaneous emission of one photon off an electron in an external e.m. wave. Evaluation of corresponding transition matrix is close to that of case of the Breit-Wheeler process because both processes are crossed to each other. Despite of the similarities of these two processes, the physical meaning of the dynamical variables and observables is quite different. For the sake of completeness, we start our analysis from fully differential cross sections which are calculated as a function of the frequency of the outgoing photon at fixed scattering angle. The main difference to the previous studies mentioned above is utilizing a wider class of the pulse envelope functions including flat-top envelopes. However, the fully differential cross section has a complicated structure being rapidly oscillating function of the energy of the outgoing photons ω' at fixed production angle θ', especially in the kinematically forbidden region. It is clear that experimental studying the multi-photon dynamics in case of rapidly varying cross sections is a challenging task. Rather integrated observables may overcome this problem.

But here one has to be careful. The totally integrated cross section is not suitable for this aim, because in this case the integration starts from the minimum value of the energy of the outgoing photon, ω'_1, kinetically allowed for the electron - one photon interaction, and this

region dominates in the total cross section, masking the relatively weak effects of electron - multi-photon interactions. To highlight the role of the multi-photon interaction the lower limit of integration ω' must be shifted relative to ω'_1: $\omega' > \omega'_1$. Such partially integrated cross sections are smooth functions of ω' and allow to study directly the multi-photon dynamics. Similarly to the variable ζ in the Breit-Wheeler process, the ratio $\kappa = \omega'/\omega'_1 > 1$ may be considered as a sub-threshold variable in non-linear Compton scattering.

We show below that in the considered quantum processes the production probability (or cross section) is determined by the non-trivial interplay of two dynamical effects. The first one is related to the shape and duration of the pulse, while the second one is the non-linear dynamics of the electron (positron) in the strong electromagnetic field, independently of the pulse geometry. These two effects play quite different roles in two limiting cases. The pulse shape effects manifest most clearly in the weak-field regime characterized by small values of the reduced field intensity ξ^2. The rapid variation of the e.m. field in very short (and, in particular, in sub-cycle) pulses enhances strongly few-photon events such that their probability may exceed the IPA result by orders of magnitude. Non-linear multi-photon dynamics of the strong electromagnetic field plays a dominant role at large values of ξ^2. In this case, results of the IPA and the FPA are close to each other. In the transition region, i.e. at intermediate values $\xi^2 \sim 1$, the observables are determined by the interplay of both effects which must be taken into account simultaneously. For the quantum processes in IPA we refer the reader to the review paper [17].

This review is based on the methods and results obtained in Refs. [25–27] and [24]. It is organized as follows. In Sect. 2 we discuss the properties of envelope functions used below. Sect. 3 is devoted to the non-linear Breit-Wheeler process for different pulse shapes, pulse durations and e.m. field intensities deriving the basic expressions for the probability of e^+e^- creation in FPA. We successively analyze cases of (i) small pulse duration with number of oscillations $N = 2...10$ at different pulse intensities, (ii) the case of large field intensity where the pulse shape becomes unessential, and (iii) sub-cycle pulses with $N < 1$, where the pulse structure is particularly important. Special attention is paid to the impact of the carrier phase. In Sect. 4 we discuss several aspects of non-linear Compton scattering for short and sub-cycle pulses. Our conclusions are presented in Sect. 5. In Appendix, for completeness and easy reference, we present some details of a derivation of the e^+e^- production probability for very high intensities, $\xi^2 \gg 1$.

II. ENVELOPE FUNCTIONS

Below, we are going to analyze dependence of observables on the shape of $f(\phi)$ in Eq. (1) for two types of envelopes: the one-parameter hyperbolic secant (hs) shape and the two-parameter symmetrized Fermi (sF) shape widely used for parametrization of the nuclear density [48]:

$$f_{\rm hs}(\phi) = \frac{1}{\cosh\frac{\phi}{\Delta}}\ , \qquad f_{\rm sF}(\phi) = \frac{\cosh\frac{\Delta}{b}+1}{\cosh\frac{\Delta}{b}+\cosh\frac{\phi}{b}}\ . \tag{8}$$

These two shapes cover a variety of relevant envelopes discussed in literature (for details see [26]). The parameter b in the sF shape describes the ramping time in the neighborhood of $\phi \sim \Delta$. Small values of ratio b/Δ cause a flat-top shaping. At $b/\Delta \to 0$, the sF shape becomes a rectangular pulse [18]. In the following, we choose the ratio b/Δ as the second independent parameter for the sF envelope function. The parameter Δ characterizes the pulse duration 2Δ with $\Delta = \pi N$, where N has a meaning of a "number of oscillations" in the pulse. Certainly, such a definition is rather conditional and is especially meaningful for the flat-top envelope with small values of b/Δ. In the case of the hs envelope shape, the number of oscillations with small amplitudes may exceed N. Nevertheless, for convenience we call N as a "number of oscillations in a pulse" for given $f(\phi)$, relying on its relation to the shape parameter Δ. It was shown that the properties of the two-parameter sF shape for large values of $b/\Delta \simeq 0.3 \ldots 0.5$ are close to that of the one-parameter hs shape. Therefore, as mentioned above, in order to stress the difference between one- and two-parameter (flat-top) envelopes we focus our consideration on the choice of $b/\Delta = 0.15$ throughout present paper.

The envelope shape $f(\phi)$ and the integrand $f^2(\phi) + f'^2(\phi)$ (which is proportional to the square of the e.m. field strength) in Eq. (6) as functions of the invariant phase for hs and sF shapes are shown in Fig. 2 in left and right panels, respectively. The numbers in the plot indicate the number of oscillations in a pulse N. The thick solid curves labeled by N are for $f(\phi)$. The dashed, long-dashed, dot-dashed and dot-dot-dashed curves are for $f^2(\phi)+f'^2(\phi)$ with $N = 0.5$, 2, 5 and 10, respectively. For the smooth hs shape the integrand is also a smooth function (cf. Fig. 2, left panel). For the flat-top sF envelope shape and $N \geq 2$ both, $f(\phi)$ and the integrand $f^2(\phi) + f'^2(\phi)$ are smooth functions of the invariant phase which is more compact as compared with the hs shape with the same value of N. At $N = 0.5$ and

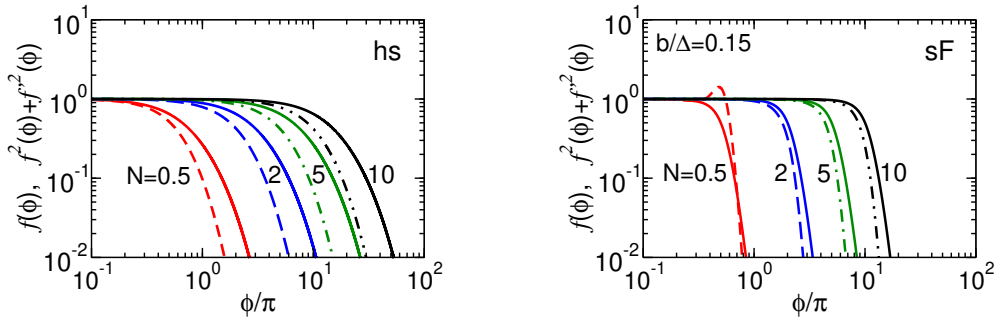

FIG. 2: The envelope functions $f(\phi)$ and the integrand $f^2(\phi)+f'^2(\phi)$ in Eq. (6) as the functions of the invariant phase $\phi = kx$. The thick solid curves labeled by N are for $f(\phi)$. The dashed, long-dashed, dot-dashed and dot-dot-dashed curves are for $f^2(\phi)+f'^2(\phi)$ with $N = 0.5$, 2, 5 and 10, respectively. Left and right panels are for hs and sF envelope shapes, respectively.

$\phi \sim \Delta$ the integrand (see dashed curve in the right panel) displays some overshoot resulting locally in the height $h = 1/4 + (\frac{\Delta}{b}/4\Delta)^2 \simeq 1.37$. Increasing Δ (or b/Δ) leads to a vanishing of this overshoot.

For the hs envelope, the normalization factor in Eq. (6) has the form

$$N_0^{\rm hs} = \frac{\Delta}{\pi}\left(1+\frac{1}{3\Delta^2}\right) \ , \tag{9}$$

while for the sF shape the normalization factor reads

$$N_0^{\rm sF} = \frac{\Delta}{\pi}\left(F_1\left(t\right)+F_2\left(t\right)\frac{b}{\Delta}\right), \ \ t=\frac{1+\cosh\frac{\Delta}{b}}{\sinh\frac{\Delta}{b}} \ , \tag{10}$$

where

$$\begin{aligned} F_1(t) &= \frac{(t^2+1)(-t^4+10t^2-1)}{16t} \ , \\ F_2(t) &= \frac{3t^{10}-35t^8+90t^6-90t^4+35t^2-3}{24(t^2-1)^3} \ . \end{aligned} \tag{11}$$

In the limit $\frac{b}{\Delta} \to 0$,

$$N_0^{\rm sF} = \frac{\Delta}{\pi} + \mathcal{O}\left(\exp[-\frac{\Delta}{b}]\right) \simeq \frac{\Delta}{\pi}. \tag{12}$$

The normalization factor N_0 scaled by $N = \Delta/\pi$ as a function of N for hs and sF shapes is exhibited in Fig. 3, shown by the dashed and solid curves, respectively.

For the hs shape, $N_0 \simeq N$ at $N \geq 1$ and slightly increases for the sub-cycle envelopes with $N < 1$ (cf. Eq. (9)). In case of a flat-top envelope, the ratio N_0/N is independent of Δ,

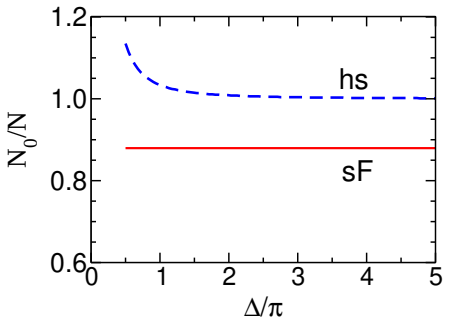

FIG. 3: The scaled normalization factor N_0/N as a function of the number of oscillations in the pulse, $N = \Delta/\pi$, for hs and sF shapes, shown by the dashed blue and solid red curves, respectively.

according to Eq. (11). The contribution of f'^2 in (6) is weak and varies from 0.2% to 3.8% for $b/\Delta = 0.01$ and 0.2, respectively. In the limit $b/\Delta \to 0$ it vanishes and $N_0 \to N$ and therefore, the overshoot in the integrand does not affect the integral in Eq. (6). But taking into account that very small values of b/Δ seems to be not realistic, we restrict our actual calculations to the finite value $b/\Delta = 0.15$, where the overshoot in $f^2(\phi) + f'^2(\phi)$ is minor.

For the sake of completeness, we present also the behavior of e.m. potential $\mathbf{A}$ and the electric field strength $\mathbf{E} = -\partial\mathbf{A}/\partial t$, where $\mathbf{A}$ is given by Eqs. (1) and (8) as functions of the invariant phase ϕ. The e.m. potential and strength for the one- and two-parameter envelope functions read

$$A_x = a\, f(\phi)\cos\phi\ , \qquad A_y = a\, f(\phi)\sin\phi\ , \tag{13}$$

$$E_x = \omega\, A_x\left[-(\ln f(\phi))' + \tan\phi\right]\ , \tag{14}$$

$$E_y = \omega\, A_y\left[-(\ln f(\phi))' - \cot\phi\right]\ , \tag{15}$$

with $a = |\,\mathbf{a}_1| = |\,\mathbf{a}_2|$ and

$$-\,(\ln f(\phi))' = \begin{cases} \frac{1}{\Delta}\tanh\frac{\phi}{\Delta}, & \text{hs}, \\ \frac{1}{b}\frac{\sinh\frac{\phi}{b}}{\cosh\frac{\Delta}{b}+\cosh\frac{\phi}{b}}, & \text{sF}. \end{cases} \tag{16}$$

The scaled potentials A_x/a and the scaled strengths $E_x/a\omega$ as functions of the invariant phase are exhibited by solid and dashed curves, respectively, in upper and middle panels in Fig. 4 for the hs and sF shapes. The left and right panels correspond to the pulses with $N = 2$ and 0.5, respectively. The result for the hs shape with $N = 0.5$ is close qualitatively

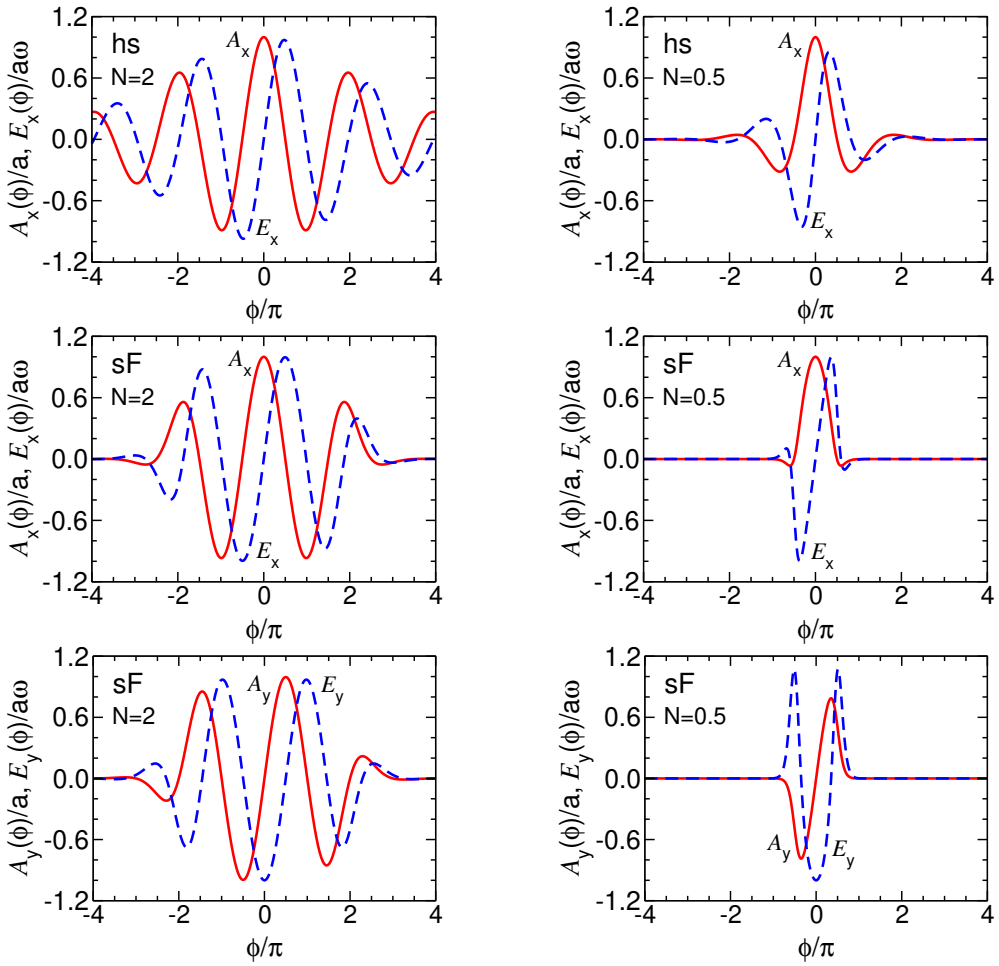

FIG. 4: The e.m. potentials A/a (solid curves) and field strengths $E/a\omega$ (dashed curves) as functions of the invariant phase ϕ. The upper and middle panels correspond to the hyperbolic secant (hs) and symmetrized Fermi (sF) shapes, respectively, for the x components. The lower panels correspond to the y components for the sF envelope shape. The left and right panels are for pulses with $N = 2$ and $N = 0.5$, respectively.

to that of [10]. One can see that the duration of the pulse increases with increasing number of oscillations. The flat-top sF shape is more compact compared to the hs shape with the same value of the pulse "scale" parameter Δ.

The result for y components is exhibited in Fig. 4, lower panels, where we restrict ourselves to the example of the flat-top sF envelope shape. For short pulses with $N > 2$, the contribution of the first terms in Eqs. (14) and (15) are relatively small and, therefore, the approximate relations $A_y \simeq E_x/\omega$ and $E_y \simeq -\omega\, A_x$ are valid. Both A_y and E_y are finite.

The same is true for the sF shape with $N \geq 2$. This is illustrated in Fig. 4, lower panel (left), where the result for the sF envelope with $N = 2$ is shown. The approximate relations are valid also for sub-cycle pulse with $N = 0.5$ and for the one-parameter hs shape. In case of the flat-top envelope for $N = 0.5$, the above approximate relations are valid for A_y and for the central part of E_y (cf. Fig. 4 lower panel (right)). In the border area with $\phi \approx \Delta = \frac{\pi}{2}$, the strength E_y has finite narrow peaks with height $\tilde{h} = \left(\frac{\Delta}{b}\right) \frac{\sin \Delta}{4\Delta} + \mathcal{O}(\exp(-\Delta/b)) \simeq 1.06$. The height of these peaks decreases with increasing Δ at fixed b/Δ and for $N \geq 2$ it becomes negligibly small. This "pick-like" behavior for the flat-top shape can be compared with the the popular rectangular pulse [18] where the derivative $f'(\phi) = \theta'(\phi - \Delta) = \delta(\phi - \Delta)$ is singular at $\phi = \Delta$. But such "pick-like" or even singular behavior of $\mathbf{E}$ at the border does not affect the transition matrix elements, discussed in the next section (cf. Eq. (18)), since they are determined by $\mathbf{A}$ and $\mathbf{A}^2$ rather than the e.m. strength. Therefore, our plots and discussions for the e.m. strength $E_{x,y}$ have an illustrative character since the dynamics of the considered process is determined purely by the e.m. potential $A_{x,y}$, which is taken, in our approach, as a primary quantity.

III. THE e^+e^- PAIR PRODUCTION IN A FINITE PULSE

A. General formalism

In our consideration of quantum processes, we start from e^+e^- pair production in the interaction of a probe photon with a circularly polarized e.m. field described by Eq. (1). Within the Furry picture, the process is diagrammatically represented by a one-vertex graph, describing the decay of the probe photon with the four-momentum k' into a laser dressed e^+e^- pair, where the presence of the background e.m. field is included in the Volkov solution of the outgoing e^+ and e^-. (In the weak-field approximation this graph turns into the known two two-vertex graphs for the perturbative Breit-Wheeler process). Utilization of (1) leads to two significant modifications of the transition amplitude in FPA compared to IPA. In IPA, the Volkov solutions [49, 50] refer to fermions with quasi-momenta $q_\mu = p_\mu + k_\mu \frac{\xi^2 m^2}{2(k\cdot p)}$ and dressed masses $m_*^2 = m^2(1 + \xi^2)$. In FPA, all fermion momenta and masses take their vacuum values p and m, respectively, whereas the corresponding wave functions are modified in accordance with the Volkov solution (with more complicated compare to IPA,

phase factor). The finite (in space-time) e.m. potential (1) for FPA requires the use of Fourier integrals for invariant amplitudes, instead of Fourier series which are employed in IPA. The partial harmonics become thus continuously in FPA. The S matrix element is expressed generically as

$$S_{fi} = \frac{-ie}{\sqrt{2p_0 2p_0' 2\omega'}} \int_{\zeta}^{\infty} dl\, M_{fi}(l)(2\pi)^4 \delta^4(k' + lk - p - p'), \tag{17}$$

where k, k', p and p' refer to the four-momenta of the background (laser) field (1), incoming probe photon, outgoing positron and electron, respectively, the low limit ζ is defined in Eq. (7). The transition matrix $M_{fi}(l)$ consists of four terms

$$M_{fi}(l) = \sum_{i=0}^{3} M^{(i)}\, C^{(i)}(l)\ , \tag{18}$$

where

$$\begin{aligned}
C^{(0)}(l) &= \frac{1}{2\pi} \int_{-\infty}^{\infty} d\phi\, \mathrm{e}^{il\phi - i\mathcal{P}(\phi)}\ , \\
C^{(1)}(l) &= \frac{1}{2\pi} \int_{-\infty}^{\infty} d\phi f^2(\phi)\, \mathrm{e}^{il\phi - i\mathcal{P}(\phi)}\ , \\
C^{(2)}(l) &= \frac{1}{2\pi} \int_{-\infty}^{\infty} d\phi f(\phi)\, \cos\phi\, \mathrm{e}^{il\phi - i\mathcal{P}(\phi)}\ , \\
C^{(3)}(l) &= \frac{1}{2\pi} \int_{-\infty}^{\infty} d\phi f(\phi)\, \sin\phi\, \mathrm{e}^{il\phi - i\mathcal{P}(\phi)}\ ,
\end{aligned} \tag{19}$$

with

$$\mathcal{P}(\phi) = z \int_{-\infty}^{\phi} d\phi'\, \cos(\phi' - \phi_0) f(\phi') - \xi^2 \zeta u \int_{-\infty}^{\phi} d\phi'\, f^2(\phi')\ . \tag{20}$$

The quantity z is related to ξ, l, and $u \equiv (k' \cdot k)^2 / \left(4(k \cdot p)(k \cdot p')\right)$ via

$$z = 2l\xi \sqrt{\frac{u}{u_l}\left(1 - \frac{u}{u_l}\right)} \tag{21}$$

with $u_l \equiv l/\zeta$. The phase ϕ_0 is equal to the azimuthal angle of the direction of flight of the outgoing electron in the e^+e^- pair rest frame $\phi_0 = \phi_{p'} \equiv \phi_e$ and it is related to

the azimuthal angle of the positron momentum as $\phi_0 = \phi_{e^+} + \pi$. Similarly to IPA, it can be determined through invariants $\alpha_{1,2}$ as $\cos\phi_0 = \alpha_1/z$, $\sin\phi_0 = \alpha_2/z$ with $\alpha_{1,2} = e\,(a_{1,2}\cdot p/k\cdot p - a_{1,2}\cdot p'/k\cdot p')$.

The transition operators $M^{(i)}$ in Eq. (18) have the form

$$M^{(i)} = \bar{u}_{p'}\,\hat{M}^{(i)}\,v_p \tag{22}$$

with

$$\begin{aligned}\hat{M}^{(0)} &= \not{\varepsilon}'\ , \quad \hat{M}^{(1)} = -\frac{e^2a^2\,(\varepsilon'\cdot k)\,\not{k}}{2(k\cdot p)(k\cdot p')}\ ,\\ \hat{M}^{(2,3)} &= \frac{e\not{a}_{(1,2)}\not{k}\not{\varepsilon}'}{2(k\cdot p')} - \frac{e\not{\varepsilon}'\not{k}\not{a}_{(1,2)}}{2(k\cdot p)}\ .\end{aligned} \tag{23}$$

where $u_{p'}$ and v_p are the Dirac spinors of the electron and positron, respectively, and ε' is the polarization four-vector of the probe photon.

The integrand of the function $C^{(0)}$ in Eqs. (19) does not contain the envelope function $f(\phi)$ and therefore it is divergent. One can regularize it by using the prescription of Ref. [18] which leads to

$$\begin{aligned}C^{(0)}(l) &= \frac{1}{2\pi l}\int\limits_{-\infty}^{\infty} d\phi\,\left(z\cos(\phi-\phi_0)\,f(\phi) - \xi^2\zeta u\,f^2(\phi)\right)\,\mathrm{e}^{il\phi - i\mathcal{P}(\phi)}\\ &\quad + \delta(l)\,\mathrm{e}^{-i\mathcal{P}(0)}\ .\end{aligned} \tag{24}$$

This expression contains a singular (last) term which however, does not contribute because of kinematical restriction, implying $l > 0$.

The differential probability of e^+e^- pair production in terms of the transition matrix $M_{fi}(l)$ in Eq. (17) reads

$$dW = \frac{\alpha\zeta^{1/2}}{2\pi N_0 m}\int\limits_{\zeta}^{\infty} dl\ |M_{fi}(l)|^2\,\frac{d\mathbf{p}}{2p_0}\,\frac{d\mathbf{p}'}{2p_0'}\delta^4(k'+lk-p-p')\ . \tag{25}$$

It may be represented in conventional form as a function of u and ϕ_e

$$\frac{dW}{d\phi_e\,du} = \frac{\alpha m\zeta^{1/2}}{16\pi N_0}\,\frac{1}{u^{3/2}\sqrt{u-1}}\int\limits_{\zeta}^{\infty} dl\ w(l) \tag{26}$$

with

$$\begin{aligned}\frac{1}{2}\,w(l) &= (2u_l+1)|C^{(0)}(l)|^2 + \xi^2(2u-1)(|C^{(2)}(l)|^2 + |C^{(3)}(l)|^2)\\ &\quad + \mathrm{Re}\,C^{(0)}(l)\left(\xi^2C^{(1)}(l) - \frac{2z}{\zeta}(\cos\phi_0 C^{(2)}(l) + \sin\phi_0 C^{(3)}(l))\right)^*\ .\end{aligned} \tag{27}$$

The normalization factor N_0 is determined by Eq. (6) and has been discussed in the previous section.

It is convenient to express the $C^{(i)}(l)$ functions defined in Eqs. (19) and (24) through the new, basic functions Y_l and X_l, which may be considered as an analog of the Bessel functions in IPA,

$$\begin{aligned} Y_l(z) &= \frac{1}{2\pi}\mathrm{e}^{-il\phi_0}\int\limits_{-\infty}^{\infty} d\phi\, f(\phi)\,\mathrm{e}^{il\phi - i\mathcal{P}(\phi)}\ , \\ X_l(z) &= \frac{1}{2\pi}\mathrm{e}^{-il\phi_0}\int\limits_{-\infty}^{\infty} d\phi\, f^2(\phi)\,\mathrm{e}^{il\phi - i\mathcal{P}(\phi)}\ . \end{aligned} \tag{28}$$

The new representation of the basic functions $C^{(i)}(l)$ reads

$$\begin{aligned} C^{(1)}(l) &= X_l(z)\,\mathrm{e}^{il\phi_0}\ , \\ C^{(2)}(l) &= \frac{1}{2}\left(Y_{l+1}\mathrm{e}^{i(l+1)\phi_0} + Y_{l-1}\mathrm{e}^{i(l-1)\phi_0}\right)\ , \\ C^{(3)}(l) &= \frac{1}{2i}\left(Y_{l+1}\mathrm{e}^{i(l+1)\phi_0} - Y_{l-1}\mathrm{e}^{i(l-1)\phi_0}\right)\ , \\ C^{(0)}(l) &= \widetilde{Y}_l(z)\mathrm{e}^{il\phi_0},\ \widetilde{Y}_l(z) = \frac{z}{2l}\left(Y_{l+1}(z) + Y_{l-1}(z)\right) - \xi^2\frac{u}{u_l}X_l(z)\ . \end{aligned} \tag{29}$$

It allows to express $w(l)$ in Eq. (27) in the form

$$w(l) = 2\widetilde{Y}_l^{\,2}(z) + \xi^2(2u-1)\left(Y_{l-1}^2(z) + Y_{l+1}^2(z) - 2\widetilde{Y}_l(z)X_l^*(z)\right)\ , \tag{30}$$

which resembles the expression for the probability in case of IPA

$$w_n = 2J_n^2(z) + \xi^2(2u-1)\left(J_{n-1}^2(z) + J_{n+1}^2(z) - 2J_n^2(z)\right)\ , \tag{31}$$

with the substitution $\widetilde{Y}_l^{\,2}(z) \to J_n^2(z)$, $Y_{l\pm1}^2(z) \to J_{n\pm1}^2(z)$, and $\widetilde{Y}_l(z)X_l^*(z) \to J_n^2(z)$.

The differential probability dW in Eq. (26), is in fact, the probability per unit time (or rate), and it is related to the differential cross section $d\sigma$ as

$$dW = J\cdot\rho_\gamma\, d\sigma = 2\cdot\frac{\omega m^2\xi^2}{4\pi\alpha}\, d\sigma\ , \tag{32}$$

where $J = 2$ and ρ_γ are the flux of incoming probe photon and the density of the background photons, respectively, ω is the frequency of the background photon. Thus, the differential cross section reads

$$\frac{d\sigma}{d\phi_p\, du} = \frac{\alpha^2\zeta}{2s_{\rm thr}\xi^2 N_0}\,\frac{1}{u^{3/2}\sqrt{u-1}}\int\limits_{\zeta}^{\infty} dl\ w(l)\ . \tag{33}$$

Later, for easy reference and comparison with previous works (cf. [17]) we present our results for the Breit-Wheeler process in terms of probabilities dW (production rates) rather than the cross sections $d\sigma$, remembering Eq. (32) connecting these two observables.

B. Short pulses

In this section we consider short pulses with the number of oscillation $N \geq 2$, however, the developed methods for studying probabilities of e^+e^- pair production are valid even for pulses with $N \sim 1$. The sub-cycle pulses with $N < 1$ will be considered separately, in subsection F. Recall that we consider two envelope shapes: hyperbolic secant (hs) shape and symmetrized Fermi (sF) shape with $b/\Delta = 0.15$.

As mentioned above, Eqs. (26) and (33) with Eq. (27) can be used for numerical estimates of the e^+e^- production probability or cross section evaluating five dimensional integral(s) with rapidly oscillating functions. Technically, such an approach needs long calculation time for reasonable computational accuracy which makes it difficult for applications in transport/Monte Carlo codes. However, a closer inspection of the functions $\mathcal{P}(\phi)$ and Y_l, X_l shows that the number of integrations may be reduced and, in some cases, Eq. (30) may be expressed in an analytical form. Thus, integrating by parts the function $\mathcal{P}(\phi)$ might be rewritten in the following form

$$\begin{aligned} \mathcal{P}(\phi) \;&\equiv\; \mathcal{P}_0(\phi) - \xi^2\zeta u \int\limits_{-\infty}^{\phi} d\phi'\, f^2(\phi') \;, \\ \mathcal{P}_0(\phi) \;&=\; z\,\left(\sin(\phi-\phi_0) f(\phi) + \mathcal{O}\left(\frac{1}{\Delta}\right)\right) \end{aligned} \tag{34}$$

with

$$\mathcal{O}\left(\frac{1}{\Delta}\right) = -\frac{1}{\Delta}\int\limits_{-\infty}^{\phi} d\phi'\, \sin(\phi'-\phi_0) f'(\phi') \;. \tag{35}$$

The contribution of this term to $\mathcal{P}(\phi)$ is sub leading for the finite pulse size $\Delta = \pi N$ with $N \geq 2$. First, because of the explicit factor $1/\Delta$, and second because the derivative $f'(\phi)$ in the integrand reaches its maximum value at the boundaries of the pulse, where this function is suppressed. For an illustration, in Fig. 5 we present results of a numerical analysis of $\mathcal{P}_0(\phi)$ with the hyperbolic secant envelope function. The solid and dashed curves exhibit

calculations with and without the term (35), respectively for $\phi_0 = 0$ and π. The left and right panels correspond to $\Delta = \pi N$ with $N = 2$ and 5, respectively. The term ($|\mathcal{O}(1/\Delta)|$) is shown by dot-dashed curves. One can see, in fact, that this term is rather small and may

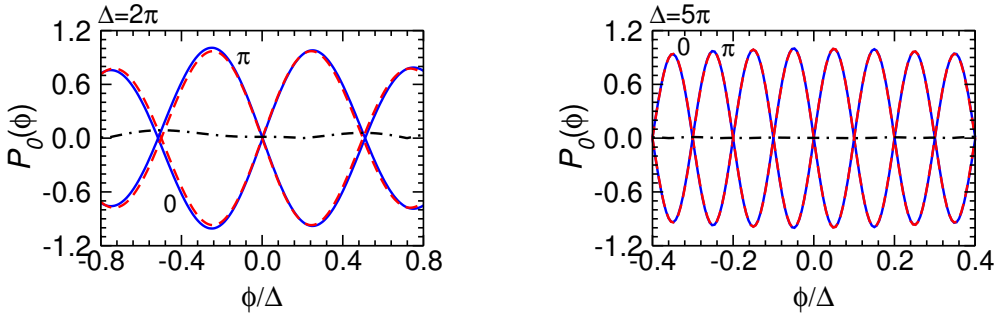

FIG. 5: The function $\mathcal{P}_0(\phi)$ defined in (34) with (solid curves) and without (dashed curves) the term (35) for $\Delta = \pi N$ with $N = 2$ and 5, shown in left and right panels, respectively. The term (35) is shown separately by dot-dashed curves.

be omitted. The second term in expression for $\mathcal{P}(\phi)$ in Eq. (34) is a smooth function of ϕ and in case of hs shape it can be given explicitly as $-\xi^2\zeta u\Delta\tanh(\phi/\Delta)$.

Now we are going to discuss separately the weak-, intermediate- and strong-field regimes.

C. Pair production at small field intensities ($\xi^2 \ll 1$)

In case of small $\xi^2 \ll 1$, implying $z < 1$, we decompose $l = n + \epsilon$, where n is the integer part of l, yielding

$$Y_l \simeq \frac{1}{2\pi}\int\limits_{-\infty}^{\infty} d\psi\, \mathrm{e}^{il\psi - iz\sin\psi\, f(\psi+\phi_0)} f(\psi+\phi_0)$$
$$= \frac{1}{2\pi}\int\limits_{-\infty}^{\infty} d\psi \sum_{m=0}^{\infty} \frac{(iz)^m}{m!}\sin^m\psi\, \mathrm{e}^{i(n+\epsilon)\psi} f^{m+1}(\psi+\phi_0)\ . \qquad (36)$$

Similarly, for the function $X_l(z)$ the substitution $f^{m+1} \to f^{m+2}$ applies. The dominant contribution to the integral in (36) with rapidly oscillating integrand comes from the term with $m = n$, which results in

$$Y_{n+\epsilon} \simeq \frac{z^n}{2^n n!}\,\mathrm{e}^{-i\epsilon\phi_0} F^{(n+1)}(\epsilon)\ , \qquad X_{n+\epsilon} \simeq \frac{z^n}{2^n n!}\,\mathrm{e}^{-i\epsilon\phi_0} F^{(n+2)}(\epsilon)\ , \qquad (37)$$

where the function $F^{(n)}(\epsilon)$ is the Fourier transform of the function $f^n(\psi)$.

As an example, let us analyze the e^+e^- production near the threshold, i.e. $\zeta \sim 1$. In this case, the contribution with $n = 1$ is dominant and, therefore, the functions $Y_{0+\epsilon}$ are crucial, including the first term in (30). The functions $X_{0+\epsilon}$ are not important because they are multiplied by the small ξ^2 and may be omitted. Negative $\epsilon = \zeta - 1$ and positive ϵ correspond to the above- and sub-threshold pair production, respectively. The function $Y_{0+\epsilon}$ reads $Y_{0+\epsilon} = F^{(1)}(\epsilon)\,\exp[-i\phi_0\epsilon]$, where the Fourier transforms $F^{(1)}(x)$ for the hs and sF envelope functions are equal to

$$\begin{aligned} F_{\rm hs}(x) &= \frac{\Delta}{2\cosh\frac{1}{2}\pi\Delta x}\ , \\ F_{\rm sF}(x) &= \frac{1+\exp\left[-\frac{\Delta}{b}\right]}{1-\exp\left[-\frac{\Delta}{b}\right]}\,\frac{b\,\sin\Delta l}{\sinh\pi b x}\ . \end{aligned} \tag{38}$$

The ϕ_0 dependence of the production probability disappears in this case because the latter one is determined by the quadratic terms of the Y functions.

Consider first the pair production above the threshold. Keeping the terms with leading power of ξ^2 one can express the production probability as

$$\frac{dW}{du} = \frac{\alpha M_e \zeta^{1/2}}{4N_0}\,\left[\frac{u}{u_1}\left(1-\frac{u}{u_1}\right)+u-\frac{1}{2}\right]\frac{\xi^2}{u^{3/2}\sqrt{(u-1)}}\,I_0\ , \tag{39}$$

where, taking into account that at finite values of Δ, Fourier transforms for all considered envelopes decrease rapidly with increasing ϵ, and one can gets

$$I_0 \simeq \int\limits_{1-\zeta}^{1/2} d\epsilon\, F^{(1)2}(\epsilon) \simeq \int\limits_{-\infty}^{\infty} d\epsilon\, F^{(1)2}(\epsilon) = \frac{1}{2\pi}\int\limits_{-\infty}^{\infty} d\phi\, f^2(\phi) \simeq N_0\ . \tag{40}$$

Combining these two equations one recovers the IPA result [17]. Thus, we can conclude that for small field intensities for a finite pulse duration the probabilities of e^+e^- pair emission above threshold with $\zeta < 1$ in IPA and FPA coincide, independently of the shape of the envelope function. For an illustration, in Fig. 6 we show the partial probability $w(l)$, calculated at $u = 1$ for the above-threshold region with $\xi = 10^{-2}$ and $\zeta = 0.5$ in a finite region of l for the envelope size $\Delta = \pi N$ with $N = 2$ and 10, respectively. For the envelope with a hyperbolic secant shape (left panel) one can see smooth curves with maxima at integer values of l. The widths of bumps decrease with increasing N. However, the integral of $w(l)$ over l in the neighborhood of the first maximum is independent of N and coincides with the contribution of the first harmonic in IPA which leads to an equality of IPA and FPA

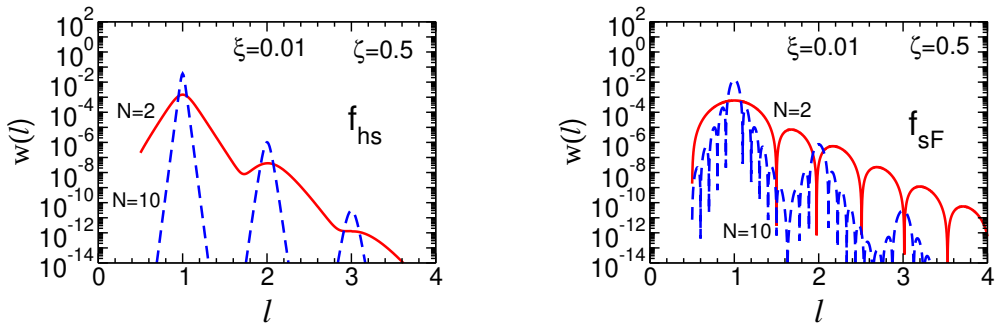

FIG. 6: The partial probability $w(l)$ defined in (30) as a function of l at $u = 1$. The solid and dashed curves correspond to the parameter $\Delta = \pi N$ with $N = 2$ and 10, respectively. Left and right panels exhibit results for the envelopes with hyperbolic secant and symmetrized Fermi shapes, respectively. For $\xi^2 = 10^{-4}$ and $\zeta = 0.5$.

results. For the symmetrized Fermi shape (right panel) the situation is different in some sense. The corresponding Fourier transforms $F_{sF}^{(n)}(l)$ in (37) oscillate with l. For example, the function $F_{sF}^{(1)}$ goes to zero at a multiple of $1/N$. This results in an oscillating structure of $w(l)$. However, the exponential decrease of $w(l)$ with increasing of the integer values of l is the same.

The situation changes when we are slightly below threshold, i.e. $\zeta > 1$. In this case, the function $Y_{0+\epsilon}$ dominates again and the result for FPA is the same as in (39) but with the substitution $I_0 \to I_1$, with $I_1 \simeq \int\limits_{\zeta-1}^{1} d\epsilon\, F^{(1)2}(\epsilon)$. In the case of smooth envelope shape (e.g. hyperbolic secant) the dominating contribution to this integral comes from the lower limit and, therefore, $I_1 \sim \left(F_{\rm hs}^{(1)}(\zeta-1)\right)^2$. As a result, the production probability strongly depends on the duration Δ of the pulse. In the case of a flat-top envelope, we have a similar effect, because $F_{sF}^{(1)}(l)$ in general, decreases exponentially as $\exp(-\pi b l)$, where b increases with increasing N at fixed b/Δ.

In Fig. 7 we show the partial probability $w(l)$ in the sub-threshold region with $\zeta = 1.25$. One can see that for the hyperbolic secant envelope (left panel) the difference of $w(l)$ at $l \simeq \zeta$ for $N = 2$ and $N = 10$ is more than several orders of magnitude, which will be reflected in the total probability. In the case of the symmetrized Fermi envelope shape, one also can see a significant enhancement of $w(l)$ for $N = 2$ compared to $N = 10$. But now, the difference between FPA and IPA is larger compared to the case of the hyperbolic secant shape.

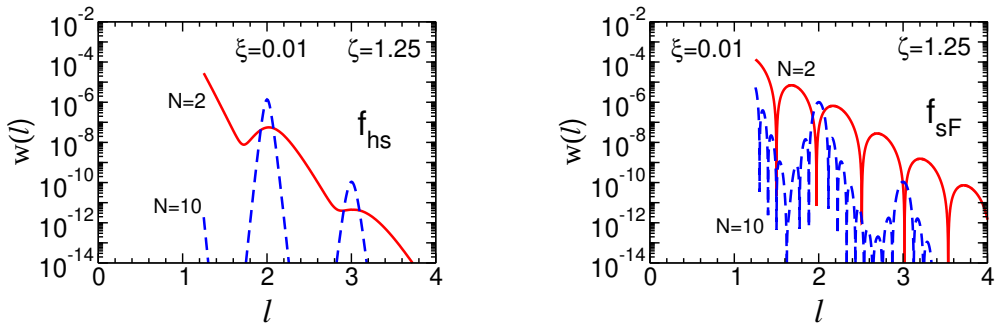

FIG. 7: The same as in Fig. 6 but for the sub-threshold region at $\zeta = 1.25$.

The total probability W of e^+e^- emission as a function of the sub-threshold parameter ζ in the vicinity $\zeta \sim 1$ is presented in Fig. 8. The dashed and solid curves correspond to

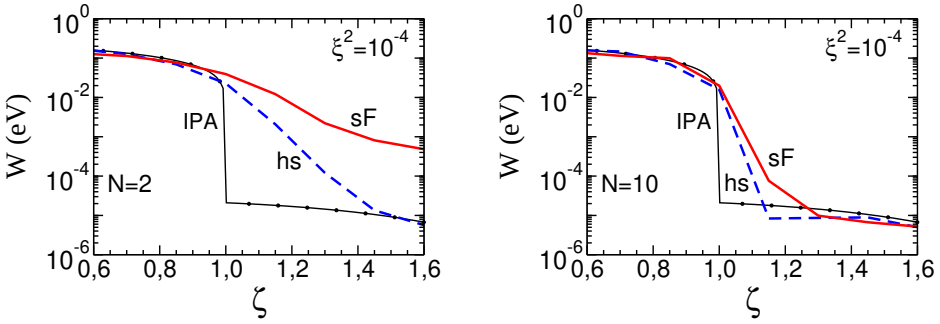

FIG. 8: The total probability W of the e^+e^- pair production as a function of ζ for short pulses with $\Delta = \pi N$ for $N = 2$, and 10 shown in the left and right panels, respectively; $\xi^2 = 10^{-4}$. The dashed and solid curves correspond to the hyperbolic secant and symmetrized Fermi envelope shapes, respectively. The thin solid curves marked by dots depict the IPA result.

the hyperbolic secant and symmetrized Fermi envelope shapes, respectively. The left and right panels correspond to the short pulses with $\Delta = \pi N$ for $N = 2$, and 10, respectively, at $\xi^2 = 10^{-4}$. For comparison, we present also the IPA results. In the above-threshold region, results of IPA and FPA are equal to each other according to Eqs. (39) and (40). However, in the sub-threshold region, where ζ is close to unity, the probability of FPA considerably exceeds (by more than two orders of magnitude) the corresponding IPA result. In the case of the hyperbolic secant envelope function, the probability increases with decreasing pulse duration. The results of FPA and IPA become comparable at $N \geq 10$. Qualitatively, this result is also valid for the case of the symmetrized Fermi distribution. However, in this

case the enhancement of the probability in FPA is much greater. This is due to the fact that the maxima in the partial probability $w(l)$ (cf. Fig. 7) decreases with increasing l in different ways for different envelope shapes. In the case of the hyperbolic secant it decreases as $\exp(-\pi\Delta l)$, whereas in case of symmetrized Fermi shape it decreases as $\exp(-2\pi b l)$. For the latter one, at $b/\Delta = 0.15$ the slope is much smaller. Such a strong gain of e^+e^- emission rate is expected for other values of ζ when ζ exceeds an integer number. This effect is illustrated in Figs. 9 and 10, where the total e^+e^- production probability W is presented in a wide region of ζ at $\xi^2 = 10^{-4}$.

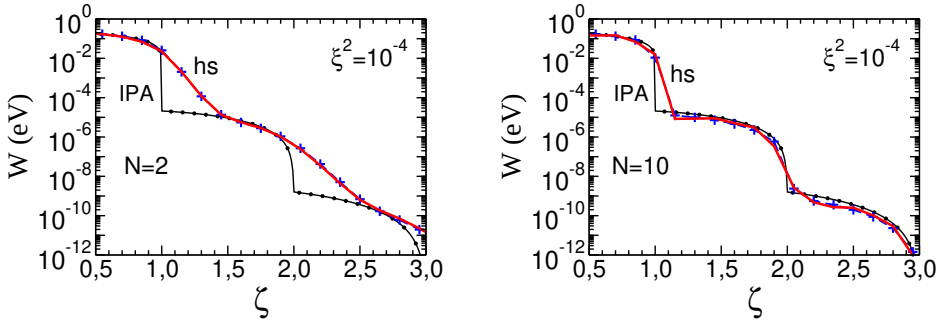

FIG. 9: The total probability W of the e^+e^- pair production as a function of ζ for the hyperbolic secant envelope shape. The solid curves are for the full calculation, while the dashed curves marked by crosses correspond to the approximate result with the basic functions taken in the form of Eq. (37). Left and right panels correspond to the number of oscillation in a pulse $N = 2$ and 10, respectively; $\xi^2 = 10^{-4}$.

In Fig. 9 we present the results for the hyperbolic secant envelope shape. The solid curves are for the full calculation, while the dashed curves marked by crosses correspond to the approximate result with the basic functions taken in the form of Eq. (37). Left and right panels correspond to the number of oscillation in a pulse $N = 2$ and 10, respectively. One can see that the approximate result is in a very good agreement with the full calculation and may be used in transport code calculations since it is much easier acceptable.

Corresponding results for the symmetrized Fermi shape envelopes are shown in Fig. 10. In the case of short pulse with $N = 2$, the approximate calculation is valid at $\zeta \lesssim 1.7$. However, when N increases, one can find agreement between full and approximate results in a wide region of ζ. For the flat-top shape with small b/Δ, the probability in FPA is larger than the result of IPA near integer values of ζ.

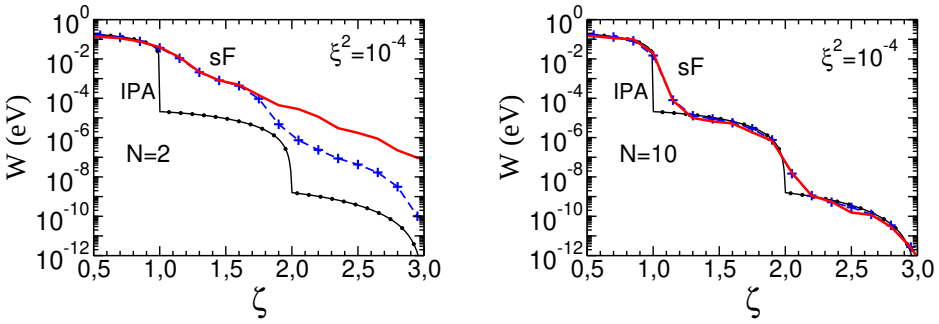

FIG. 10: The same as in Fig. 9 but for symmetrized Fermi shape.

In any case, at large values of N (right panels, $N = 10$) results of FPA and IPA become close to each other, especially for the one-parameter envelope shapes. For this case, at least for $\xi = 0.1....0.01$, $N \simeq 10$ can be considered to be near by infinite, when considering the overall ζ dependence.

To summaries this part we would like to note that temporal beam shape effects for short pulses are strong and even dominant at small field intensities in the parameter region where the variable z is small, $z < 1$. At finite z, the non-linear dynamics of e^+e^- production at high pulse intensity becomes essential.

D. The case of intermediate field intensity ($\xi^2 \sim 1$)

At finite values of z, $z \gtrapprox 1$, the probability of e^+e^- emission needs to be calculated numerically using Eqs. (26), (30), and (28). In Fig. 11, we present the total probability W as a function of ζ at fixed $\xi^2 = 1$ (left panel) and as a function of ξ^2 at fixed $\zeta = 4$ (right panel). The calculations are performed for the hyperbolic secant and symmetrized Fermi pulse envelope shapes, shown by the dashed and solid curves, respectively. The duration of the pulse is $\Delta = \pi N$ with $N = 2$. For comparison, we also present IPA results by the thin solid curves marked by dots. At finite ξ^2, the probability decreases monotonically with increasing ζ (left panel), contrary to the step-like decrease typical for the small $\xi^2 \ll 1$ (cf. Figs. 9 and 10 (right panel)).

Concerning the ξ^2 dependence (right panel), one can see a sizeable enhancement of the total probability W at small values of ξ^2 for the flat-top pulse shape compared to the case of hyperbolic secant and the IPA result. The latter two results are practically identical to

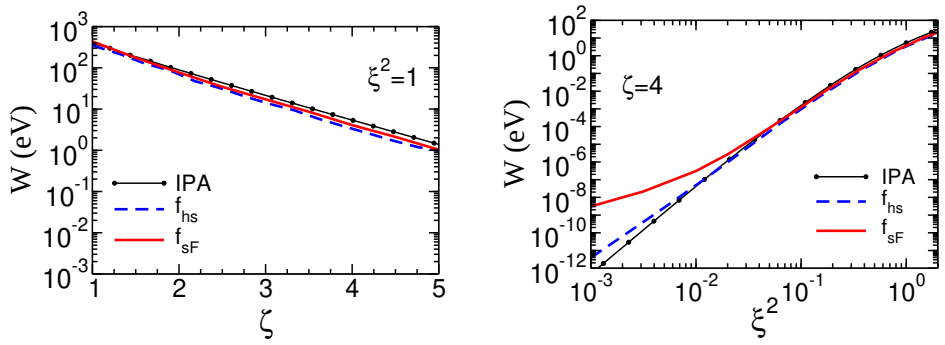

FIG. 11: The total probability of e^+e^--pair production for two envelope shapes (dashed and solid curves are for hyperbolic secant and symmetrized Fermi shapes, respectively). The thin solid curves marked by dots are the result of IPA. Left panel: The total probability as a function of ζ at $\xi^2 = 1$. Right panel: The total probability as a function of ξ^2 at $\zeta = 4$.

each other. At $\xi^2 \geq 0.1$, the production probability does not sensitively depend on the pulse shape, and FPA and IPA results are close to each other. This means that at large field intensity the dynamical aspects of the pair production gain a dominant role in comparison with the pulse shape and size effects.

Finally, we note that, at finite ξ^2, the dependence of the probability on the azimuthal angle ϕ_e disappears and the distribution in the $x - y$ plane becomes isotropic.

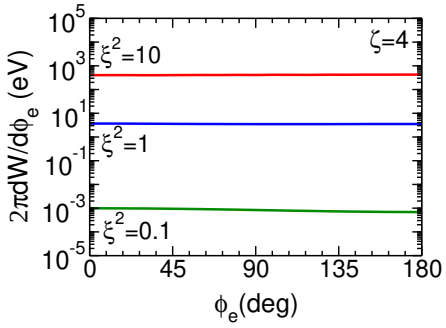

FIG. 12: The differential probability of e^+e^- pair production as a function of $\phi_{e'} = \phi_0$ at $\zeta = 4$ and $N = 2$ for different values of ξ^2.

As an example, in Fig. 12 we present prediction for the differential probability of e^+e^--pair production as a function of $\phi_e = \phi_0$ at $\zeta = 4$ for the hyperbolic secant pulse shape with $N = 2$ at $\xi^2 = 0.1$, 1 and 10. This result reflects the isotropy of the e^+e^- emission and expose the ξ^2 dependence in the considered kinematical region.

E. Pair production at large field intensity ($\xi^2 \gg 1$)

At large values of $\xi^2 \gg 1$, the basic functions Y_l and X_l in Eq. (28) can be expressed in the form of (49):

$$Y_l = \int\limits_{-\infty}^{\infty} dq\, F^{(1)}(q)\, G(l-q)\ , \qquad X_l = \int\limits_{-\infty}^{\infty} dq\, F^{(2)}(q)\, G(l-q)\ , \tag{41}$$

where $F^{(1)}(q)$ and $F^{(2)}(q)$ are Fourier transforms of the functions $f(\phi)$ and $f^2(\phi)$, respectively, and $G(l)$ may be written as

$$G(l) = \frac{1}{2\pi} \int\limits_{-\infty}^{\infty} d\phi\, \mathrm{e}^{i\left(l\phi - z\sin\phi + \xi^2\zeta u\phi\right)}\ . \tag{42}$$

In deriving this equation we have considered the following facts: (i) at large ξ^2 the probability is isotropic, therefore we put $\phi_0 = 0$, (ii) the dominant contribution to the rapidly oscillating exponent comes from the region $\phi \simeq 0$, where the difference of two large values $l\phi$ and $z\sin\phi$ is minimal, and therefore, one can decompose the last term in the function $\mathcal{P}(\phi)$ in (34) around $\phi = 0$, and (iii) replace in exponent $f(\phi)$ by $f(0) = 1$.

Equation (42) represent an asymptotic form of the Bessel functions $J_{\tilde{l}}(z)$ [51] with $\tilde{l} = l + \xi^2\zeta u$ at $\tilde{l} \gg 1$, $z \gg 1$, and therefore the following identities are valid

$$G(\tilde{l}-1) - G(\tilde{l}+1) = 2G'_z(\tilde{l}), \qquad G(\tilde{l}-1) + G(\tilde{l}+1) = 2\frac{\tilde{l}}{z}G(\tilde{l})\ , \tag{43}$$

which allow to express the partial probability $w(\tilde{l})$ in (30) as a sum of the diagonal (relative to $\tilde{l}$) terms: $Y^2_{\tilde{l}}$, $Y_{\tilde{l}}X_{\tilde{l}}$, $X^2_{\tilde{l}}$ and $Y'^2_{\tilde{l}}$. The integral over $\tilde{l}$ from the diagonal term can be expressed as

$$I_{YY} = \int\limits_{\tilde{l}_0}^{\infty} d\tilde{l}\, Y_l^2 = \int dq\, dq' F^{(1)}(q)\, F^{(1)}(q') \int\limits_{\tilde{l}_0}^{\infty} d\tilde{l} G(\tilde{l}-q)G(\tilde{l}-q')\ , \tag{44}$$

where $\tilde{l}_0 = \zeta(1+\xi^2 u$. Taking into account that for the rapidly oscillating G functions $G(l-q)G(l-q') \simeq \delta(q-q')G^2(l-q)$ and $\langle q\rangle \ll \langle l\rangle \ \sim \xi^2$ one gets

$$I_{YY} = \frac{1}{2\pi} \int\limits_{-\infty}^{\infty} d\phi f^2(\phi) \int\limits_{\tilde{l}_0}^{\infty} d\tilde{l} G^2(\tilde{l}) = N_{YY} \int\limits_{\tilde{l}_0}^{\infty} d\tilde{l} G^2(\tilde{l})\ . \tag{45}$$

Similar expressions are valid for the other diagonal terms with own normalization factors. For the $X_{\tilde{l}}^2$ term it is $N_{XX} = \frac{1}{2\pi}\int\limits_{-\infty}^{\infty} d\phi f^4(\phi)$, and for $Y_{\tilde{l}}X_{\tilde{l}}$, $N_{YX} = \frac{1}{2\pi}\int\limits_{-\infty}^{\infty} d\phi f^3(\phi)$. At large ξ^2, the probability does not depend on the envelope shape, because only the central part of the envelope is important. Therefore, for simplicity, we choose the flat-top shape with $N_{YY} = N_{YX} = N_{XX} = N_0 = \Delta/\pi$ which is valid for any smooth (at $\phi \simeq 0$) envelopes.

Making a change of the variable $l \to \tilde{l} = l + \xi^2\zeta u$ the variable z takes the following form

$$z^2 = 4\xi^2\zeta^2\left(uu_l - u^2\right) = \frac{4\xi^2 l_0^2}{1+\xi^2}\left(uu_{\tilde{l}} - u^2\right) \tag{46}$$

with $l_0 = \zeta(1+\xi^2)$ and $u_{\tilde{l}} \equiv \tilde{l}/l_0$, that is exactly the same as the variable z in IPA with the substitution $l \to \tilde{l}$. All these transformations allow to express the total probability in a form similar to the probability in IPA for large values of ξ^2 and a large number of partial harmonics n, replacing the sum over n by an integral over n [17]

$$\begin{aligned} W \;=\; & \frac{1}{2}\alpha M_e\zeta^{1/2}\int\limits_{l_0}^{\infty} d\tilde{l}\int\limits_{1}^{u_{\tilde{l}}}\frac{du}{u^{3/2}\sqrt{u-1}}\{J_{\tilde{l}}^2(z) \\ & +\; \xi^2(2u-1)[(\frac{\tilde{l}^2}{z^2}-1)J_{\tilde{l}}^2(z) + J'^2_{\tilde{l}}(z)]\}\ . \end{aligned} \tag{47}$$

Utilizing Watson's representation [51] for the Bessel functions at $\tilde{l}$, $z \gg 1$ and $\tilde{l} > z$, $J_{\tilde{l}}(z) = (2\pi\tilde{l}\tanh\alpha)^{-1/2}\exp[-\tilde{l}(\alpha - \tanh\alpha)]$ with $\cosh\alpha = \tilde{l}/z$, and employing a saddle point approximation in the integration in (47) we find the total probability of e^+e^- production as (for details see Appendix A)

$$W = \frac{3}{8}\sqrt{\frac{3}{2}}\frac{\alpha M_e\xi}{\zeta^{1/2}}\,d\,\exp\left[-\frac{4\zeta}{3\xi}(1-\frac{1}{15\xi^2})\right],\ d = 1 + \frac{\xi}{6\zeta}\left(1+\frac{\xi}{8\zeta}\right)\ . \tag{48}$$

This expression resembles the production probability in IPA which is the consequence of the fact that, at $\xi^2 \gg 1$ in a short pulse, only the central part of the envelope at $\phi \simeq 0$ is important. In case of $\xi/\zeta << 1$, approximating $d = 1 + \mathcal{O}(\xi/\zeta)$, the leading order term recovers the Ritus result [17].

For completeness, in Fig. 13 (left panel) we present FPA results of a full numerical calculation for finite values of $\xi^2 \leq 10$ for the hyperbolic secant envelope shape with $N = 2$ (curves are marked by "stars") and the asymptotic probability calculated by Eq. (48) at $\zeta = 2$, 4 and 6, shown by solid, dashed and dot-dashed curves, respectively. The transition region between the two regimes is in the neighborhood of $\xi^2 \simeq 10$. In the right panel, we

show the production probability at asymptotically large values of ξ^2 for $5 \leq \zeta \leq 20$. The exponential factor in (48) is most important at relatively low values of $\xi^2 \sim 10$ (large ζ/ξ). At extremely large values of ξ^2 (small ζ/ξ), the pre-exponential factor is dominant.

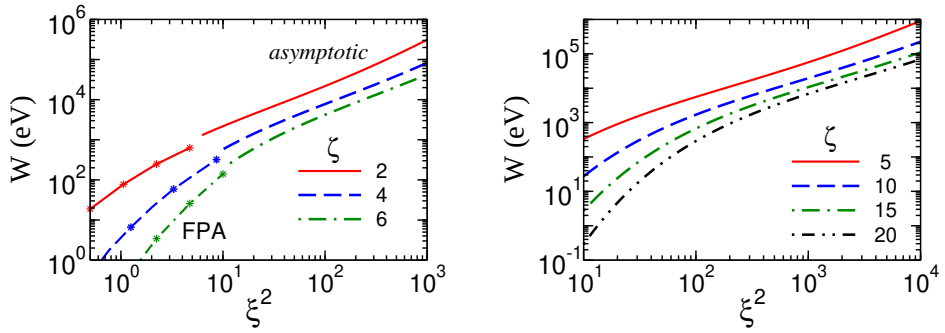

FIG. 13: The total probability W of the e^+e^- pair production as a function of ξ^2 for various values of ζ. Left panel: Results of full numerical calculation in FPA for finite values of $\xi^2 \leq 10$ (curves marked by "stars" in "FPA" sections) and the asymptotic probability (48) for large values of ξ^2 (sections labeled by "asymptotic") at $\zeta = 2$, 4 and 6. Right panel: The asymptotic probability (48) for various values of ζ as indicated in the legend.

F. Ultra-short pulses

In this section we consider e^+e^- pair production due to interaction of the probe photon with an ultra-short pulse, where the number of cycles less is than one.

1. e^+e^- pair production at small field intensity ($\xi^2 \ll 1$)

Consider first the case of small field intensity and a finite sub-threshold parameter ζ characterized by the relations $z \ll 1$ or $\xi\zeta \ll 1$.

The basic functions Y_l in Eq. (30) can be expressed in this regime as

$$Y_l = \frac{1}{2\pi} \int_{-\infty}^{\infty} d\phi \, \mathrm{e}^{il\phi} \, f(\phi) \, g(\phi) \tag{49}$$

with

$$g(\phi) \simeq \mathrm{e}^{-ic} \mathrm{e}^{-il\xi \cos\phi_0 \phi}, \tag{50}$$

where $c = z\int_{-\infty}^{0} d\phi' f(\phi')\cos(\phi'-\phi_0) - l\phi_0$ is independent of ϕ. As a result one gets

$$|Y_l| \simeq |F(l(1-\xi\cos\phi_0))| \simeq |F(l)| \ , \tag{51}$$

where $F(l)$ is the the Fourier transform of the envelope function $f(\phi)$. Keeping the leading terms in Eq. (30) with $Y_{l-1}^2 \simeq F^2(l-1)$, one can obtain an approximate expression for the total production probability:

$$W = \alpha M_e \zeta^{1/2}\xi^2 \int_{\zeta}^{\infty} dl \Phi(l)\, F^2(l-1) \ , \tag{52}$$

with

$$\Phi(l) = v\int_0^1 d\cos\theta \left(\frac{u}{u_l} - \frac{u^2}{u_l^2} + u - \frac{1}{2}\right) \ , \tag{53}$$

where $u = 1/(1-v^2\cos^2\theta)$; θ and v are the polar angle and the velocity of the outgoing electron (positron) in the e^+e^- c.m.s., respectively: $v = \sqrt{1-\zeta/l}$. An explicit calculation results in

$$\Phi(l) = \frac{1}{2}\left\{\left(1+\frac{\zeta}{l}-\frac{\zeta^2}{2l^2}\right)\log\frac{1+v}{1-v} - v\left(1+\frac{\zeta}{l}\right)\right\} \ . \tag{54}$$

The Fourier transforms of the hs and sF envelope functions are given in Eq. (38), and for illustration, the square of the Fourier transforms for a sub-cycle pulse with $N = 0.5$ are exhibited in Fig. 14. The left panel corresponds to the hyperbolic secant shape. One can see a fast monotonic decrease of $F_{\rm hs}$ at large values of l. The square of the Fourier transform for the symmetrized Fermi shape is shown in the right panel, where the solid, dashed and dot-dashed curves correspond to the ratio $b/\Delta = 0.15$, 0.3, and 0.5, respectively. One can see large qualitative and quantitative differences between the one-parameter and flat-top symmetrized Fermi shapes, in particularly, at $b/\Delta \le 0.3$. In the second case, F^2 decreases exponentially as $\exp\left[-2\pi\Delta\frac{b}{\Delta}\right]$. The slope decreases proportionally to b/Δ (at fixed Δ). Also, the function oscillates with the half-cycle $\delta\, l = \pi/\Delta = \pi/0.5\pi = 2$. Contrary to the above one-parameter shapes, the function $F_{\rm sF}$ has a significant high-l component at $2 \le l \le 4$. This strong effect is not seen in the ϕ space (cf. Fig. 4, right top and middle top panels), where all envelope functions look similar to each other. However, the difference in l-space is very important for the pair production.

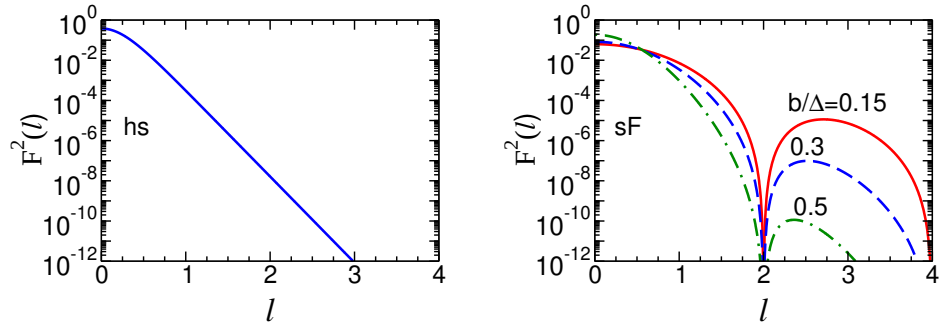

FIG. 14: Square of the Fourier transforms of the envelope functions for a sub-cycle pulse with $N = 0.5$. Left panel: The hyperbolic secant shape. Right panel: The solid, dashed and dot-dashed curves show the symmetrized Fermi shape for $b/\Delta = 0.15$, 0.3, and 0.5, respectively.

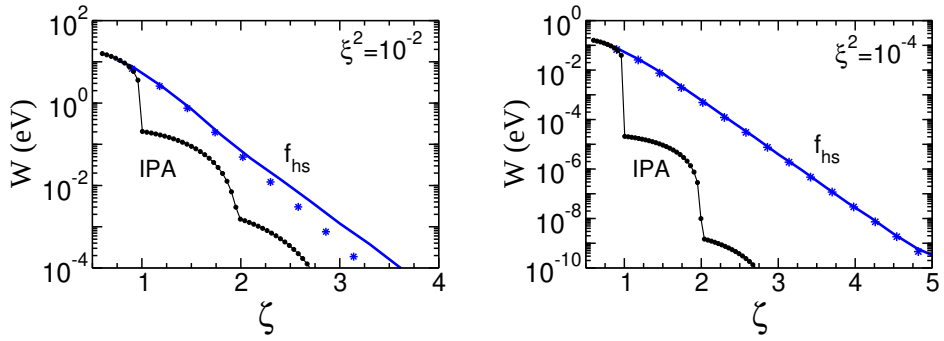

FIG. 15: The probability W of e^+e^- production as a function of the sub-threshold parameter ζ for one-parameter hs envelope functions for an ultra-short pulse with $N = 0.5$. The symbols "star" are for the approximation (52). The thin solid curves marked by dots correspond to IPA. The left and right panels are for $\xi^2 = 10^{-2}$ and 10^{-4}, respectively.

Our prediction for the total probability of e^+e^- pair production as a function of the sub-threshold parameter ζ for the one-parameter envelope functions for an ultra-short pulse with $N = 0.5$ is shown in Fig. 15. The solid curves exhibit result of full numerical calculations using Eq. (26) with the hyperbolic secant shape. The symbols "star" display the result obtained by using the approximation (52). The thin solid curves marked by dots correspond to the IPA case. The left and right panels display results for $\xi^2 = 10^{-2}$ and 10^{-4}, respectively. One can see the identity of predictions for the ultra-short pulse and IPA near and above the threshold at $\zeta \lesssim 1$, and a strong difference between them below the threshold, i.e. for $\zeta > 1$. Our approximate (analytical) solution of Eq. (52) is in a fairly good agreement with the

full numerical calculation. The function $\Phi(l)$ in Eq. (52) is rather smooth compared to the Fourier transform $F(l-1)$, therefore, the dominant contribution to the integral in Eq. (52) comes from the lower limit of l, and qualitatively, the slope of the probability as a function of ζ is determined by the scale parameter Δ of the envelope functions

$$W_{\rm hs}(\zeta) \sim \exp\left[-\pi\Delta\zeta\right] \ . \tag{55}$$

Despite of the exponential decrease of the probability W as a function of ζ, one can see a large difference (several orders of magnitude) between predictions for the ultra-short pulse and IPA. In the latter case the probability decreases much faster with increasing ζ.

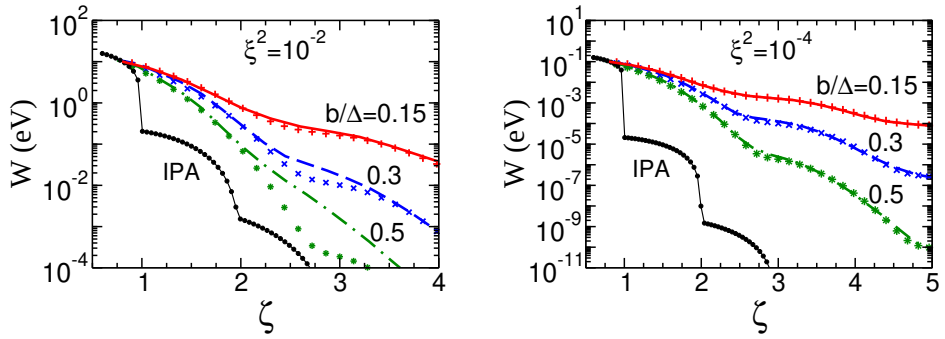

FIG. 16: The same as in Fig. 15 but for symmetrized Fermi shape envelope. The solid, dashed and dot-dashed curves are for $b/\Delta = 0.15$, 0.3 and 0.5, respectively. The corresponding approximate solutions are shown by symbols "+" , "x" and "$*$" , respectively.

Our results for the symmetrized Fermi envelope is presented in Fig. 16. Now, the shape of the probability is determined by the two parameters b (or b/Δ) and Δ

$$W_{\rm sF}(\zeta) \sim \exp\left[-2\pi\Delta\frac{b}{\Delta}\zeta\right]\sin^2\Delta\zeta \ . \tag{56}$$

The first term describes the slope of the probability as a function of ζ. The slope is proportional to the "ramping time" of the envelope function, b (or to the ratio b/Δ at fixed Δ). The second term, following from the Fourier transform shown in Fig. 14, describes some oscillations with a period inversely proportional to the duration Δ of the flat-top envelope and is independent of the ramping parameter b. Again, one can see a great difference between results for the ultra-short pulse and IPA on qualitative and quantitative levels. The probability in IPA has a typical step-like behavior, where each new step indicates the contribution

of the next integer harmonic. In FPA, the probability decreases monotonically with a slope determined by the shape of the envelope. The quantitative difference is rather large and, as indicated by results shown in Figs. 15 and 16, can reach orders of magnitude depending on the shape of the envelope.

2. Intermediate field intensity, anisotropy

As we have shown above, at small values of z, $z \ll 1$, the probability of e^+e^- production is essentially determined by the pulse shape. The function $g(\phi)$ in Eq. (49) is not important and, therefore, the total probability would be isotropic with respect to the azimuthal angle $\phi_e = \phi_0$ because only the function $\mathcal{P}(\phi)$ in Eq. (20) contains a ϕ_0 dependence. For finite values of z, however, the function $g(\phi)$ becomes important, and the electron (positron) azimuthal angle distribution is anisotropic relative to the direction of the vector $\mathbf{a}_x \equiv \mathbf{a}_1$ in Eq. (1), at least for the monotonically rapidly decreasing one-parameter envelope shapes. The reason of such anisotropy is the following. At finite values of z, the function $Y(l)$ in Eq. (49) is determined by the integral over $d\phi$ with a rapidly oscillating function proportional to the exponent in

$$\mathrm{e}^{i\left[l\phi - z\left(\cos\phi_0 \int\limits_{-\infty}^{\phi} d\phi'\, f(\phi')\cos\phi' + \sin\phi_0 \int\limits_{-\infty}^{\phi} d\phi'\, f(\phi')\sin\phi'\right)\right]} . \tag{57}$$

In the case of a fast-decreasing function $f(\phi')$, the contribution of the term proportional to $\sin\phi_0$ is much smaller compared to the term proportional to $\cos\phi_0$, because the functions $f(\phi')$ and $\sin\phi'$ in the second integral are in "anti-phase". At finite z, the dominant contribution to the functions Y_l comes from the region where the difference in the exponent is minimal, i.e. $\phi_e = \phi_0 \simeq 0$. This means that the electrons would be emitted mostly along the vector $\mathbf{a}_x$ and the positrons in the opposite direction.

We define the anisotropy of the electron emission as

$$\mathcal{A} = \frac{dW(\phi_e) - dW(\phi_e + \pi)}{dW(\phi_e) + dW(\phi_e + \pi)} . \tag{58}$$

The differential probability of the e^+e^- pair emission and the anisotropy as functions of the azimuthal angle ϕ_e are exhibited in Fig. 17. The calculations are for the fast-decreasing one-parameter hs envelope functions for $\Delta = 0.5\pi$, $\zeta = 4$ and $\xi^2 = 0.1$. One can see a rapidly

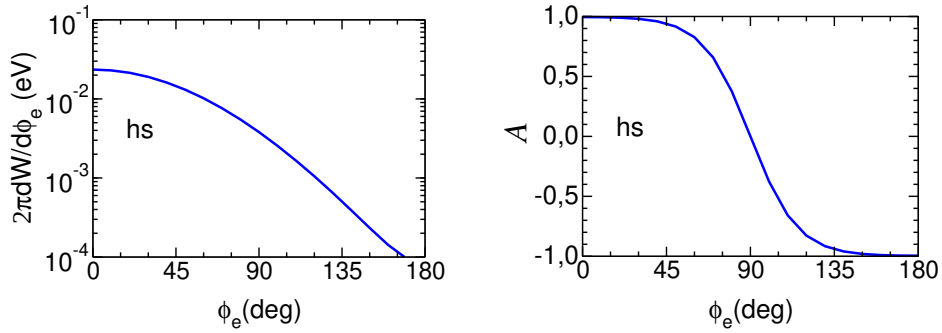

FIG. 17: Left panel: The differential production probability as a function of the azimuthal angle ϕ_e of the electron emission. Right panel: The anisotropy (58) for the hyperbolic secant shapes. For $\xi^2 = 0.1$ and $\zeta = 4$.

decreasing probability with ϕ_e which leads to the strong anisotropy of electron (positron) emission.

In the case the of the symmetrized Fermi distribution with small b/Δ, the situation changes drastically. As $b/\Delta \to 0$ the envelope function goes to the flat-top (step-like) shape $f_{\rm Fs}(\phi) \to \theta(\Delta^2 - \phi^2)$ with $\theta(x) = 1$, 0 for $x \geq 0$ or $x < 0$, respectively, and correspondingly

$$Y_l \simeq \frac{1}{2\pi} \int\limits_{-\Delta}^{\Delta} d\phi \, {\rm e}^{i\left[\tilde{l}\phi - z\sin(\phi-\phi_0)\right]} \tag{59}$$

with $\tilde{l} = l + \xi^2\zeta u$. The function Y_l in the region $\zeta \leq l < l_{\rm max} \gg 1$ is alternating, rapidly oscillating with an amplitude that depends only on ξ, ζ, and u. It is not sensitive to ϕ_0. A change in ϕ_0 leads to some phase shift of $Y(l)$ in a range of integration, leaving $\langle |Y_l|^2 \rangle$ to be independent of ϕ_0 Therefore, the dependence of the integral of the partial probability $w(l) \sim |Y_l|^2$ in Eq. (26) on ϕ_0 is negligible. As an example, in the left panel of Fig. 18 we present the partial probability $w(l)$ as a function of l, calculated at $\xi^2 = 0.1$, $\zeta = 4$ and $u = 1$ for the small values of b/Δ equal to 0.15 at $\phi_0 = 0$ and π, shown by solid and dashed curves, respectively. One can see some small modification of the frequency of oscillations at $l \sim l_{\rm min} = \zeta$ at two extreme values of ϕ_0, but the amplitudes of the oscillations are close to each other. This situation is quite different from the case of a large value of $b/\Delta = 0.5$ exhibited in the right panel of Fig. 18. One can see a strong difference in the l dependence of $w(l)$ for $\phi_0 = 0$ and π. In the first case, the function $w(l)$ has only one oscillation in a wide range of l and decreases smoothly with l. In the second case, the probability has a number of oscillations decreasing rapidly with increasing l. As a result, the total probability

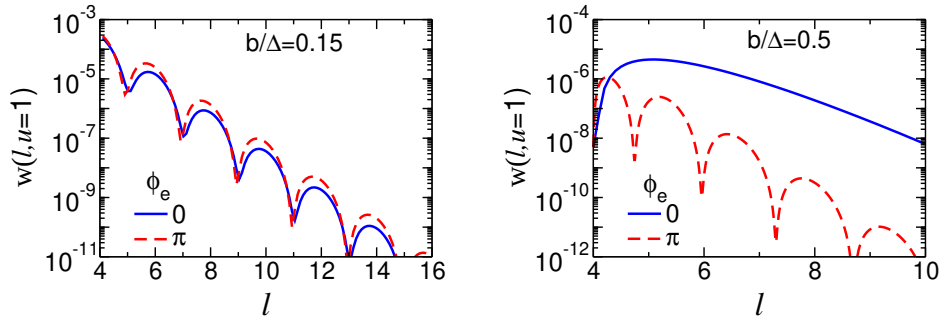

FIG. 18: The partial probability $w(l)$ defined in (30) at $\phi_0 = 0$ and π shown by solid and dashed curves, respectively, for the symmetrized Fermi envelope shape. The left panels correspond to small values of b/Δ =0.15, while the right panel is for $b/\Delta = 0.5$. For $\xi^2 = 0.1$ and $\zeta = 4$.

in the second case is much smaller.

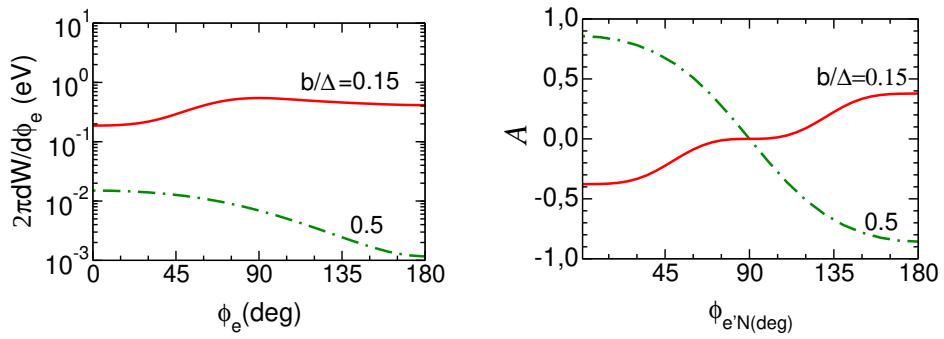

FIG. 19: The same as in Fig. 17 but for the symmetrized Fermi shape. The solid and dashed curves are for $b/\Delta = 0.15$, and 0.5, respectively.

In Fig. 19 we present our results for the symmetrized Fermi shape for the production probability (left panel) and for the anisotropy (right panel) for $b/\Delta = 0.15$, and 0.5. The result for $b/\Delta = 0.5$ is similar to that shown in Fig. 17. However, for smaller values of b/Δ, the probability is a smooth function of ϕ_e which leads to a small absolute value of the anisotropy.

G. Effect of the finite carrier phase

Consider now the impact of the finite carrier phase $\tilde{\phi}$ in the e.m. potential (1) for the e^+e^- production. In the case of finite $\tilde{\phi}$, the functions $C_l^{(i)}$ in the transition matrix (18) are

modified as follows

$$
\begin{aligned}
C^{(0)}(l) &= \frac{1}{2\pi l}\int\limits_{-\infty}^{\infty} d\phi \left(z\cos(\phi-\phi_0+\tilde{\phi})\, f(\phi) - \xi^2\zeta u\, f^2(\phi)\right) \mathrm{e}^{il\phi - i\mathcal{P}(\phi)} \ , \\
C^{(1)}(l) &= \frac{1}{2\pi}\int\limits_{-\infty}^{\infty} d\phi f^2(\phi)\, \mathrm{e}^{il\phi - i\mathcal{P}(\phi)} \ , \\
C^{(2)}(l) &= \frac{1}{2\pi}\int\limits_{-\infty}^{\infty} d\phi f(\phi)\, \cos(\phi+\tilde{\phi})\, \mathrm{e}^{il\phi - i\mathcal{P}(\phi)} \ , \\
C^{(3)}(l) &= \frac{1}{2\pi}\int\limits_{-\infty}^{\infty} d\phi f(\phi)\, \sin(\phi+\tilde{\phi})\, \mathrm{e}^{il\phi - i\mathcal{P}(\phi)} \ ,
\end{aligned} \tag{60}
$$

with

$$
\mathcal{P}(\phi) = z\int\limits_{-\infty}^{\phi} d\phi'\, \cos(\phi'-\phi_0+\tilde{\phi}) f(\phi') - \xi^2\zeta u \int\limits_{-\infty}^{\phi} d\phi'\, f^2(\phi') \ . \tag{61}
$$

Utilizing the new basic functions

$$
\begin{aligned}
Y_l(z) &= \frac{1}{2\pi}\mathrm{e}^{-il(\phi_0-\tilde{\phi})}\int\limits_{-\infty}^{\infty} d\phi\, f(\phi)\, \mathrm{e}^{il\phi - i\mathcal{P}(\phi)} \ , \\
X_l(z) &= \frac{1}{2\pi}\mathrm{e}^{-il(\phi_0-\tilde{\phi})}\int\limits_{-\infty}^{\infty} d\phi\, f^2(\phi)\, \mathrm{e}^{il\phi - i\mathcal{P}(\phi)} \ ,
\end{aligned} \tag{62}
$$

one can obtain the following representation of the functions $C^{(i)}(l)$

$$
\begin{aligned}
C^{(0)}(l) &= \widetilde{Y}_l(z)\mathrm{e}^{il(\phi_0-\tilde{\phi})} \ , \ \widetilde{Y}_l(z) = \frac{z}{2l}\left(Y_{l+1}(z)+Y_{l-1}(z)\right) - \xi^2\frac{u}{u_l}X_l(z) \ , \\
C^{(1)}(l) &= X_l(z)\, \mathrm{e}^{il(\phi_0-\tilde{\phi})} \ , \\
C^{(2)}(l) &= \frac{1}{2}\left(Y_{l+1}\mathrm{e}^{i(l+1)\phi_0} + Y_{l-1}\mathrm{e}^{i(l-1)\phi_0}\right)\mathrm{e}^{-il\tilde{\phi}} \ , \\
C^{(3)}(l) &= \frac{1}{2i}\left(Y_{l+1}\mathrm{e}^{i(l+1)\phi_0} - Y_{l-1}\mathrm{e}^{i(l-1)\phi_0}\right)\mathrm{e}^{-il\tilde{\phi}} \ ,
\end{aligned} \tag{63}
$$

which allows to express the partial probabilities $w(l)$ in Eq. (27) in the form of Eq. (30) but with the new basic functions (62). We recall that ϕ_0 in above expressions is equal to the azimuthal angle ϕ_e of the outgoing electron momentum in c.m.s..

It is naturally to expect that the effect of the finite carrier phase essentially appears in the azimuthal angle distribution of the outgoing electron because the carrier phase is included in the expressions for the basic functions (62) in the combination $\phi_e - \tilde{\phi}$.

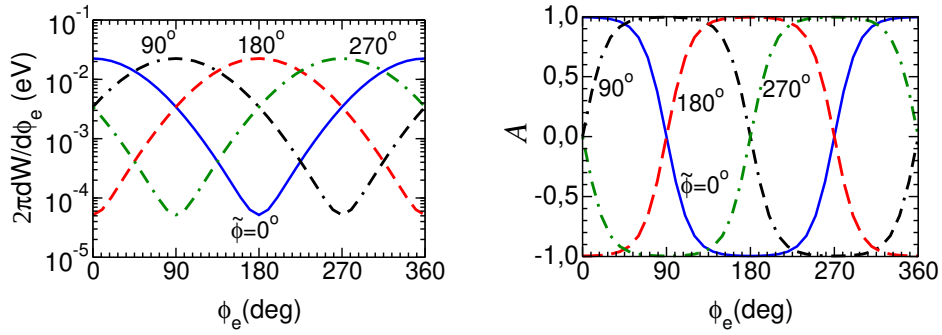

FIG. 20: Left panel: The production probability as a function of the azimuthal angle of the direction of flight of the outgoing electron ϕ_e for different values of the carrier phase $\tilde{\phi}$. The solid, dash-dash-dotted, dashed and dash-dotted curves are for the carrier phase equal to 0, 90, 180 and 270 degrees, respectively. Right panel: The anisotropy (58) for different values of $\tilde{\phi}$. For the hyperbolic secant shape with $N = 0.5$; $\xi^2 = 0.1$ and $\zeta = 4$.

As an example, in Fig. 20 (left panel) we show the probability of e^+e^- production as a function of the azimuthal angle ϕ_e for different values of the carrier phase $\tilde{\phi}$ for the sub-cycle pulse with $N = 0.5$ for a hyperbolic secant shape with $\zeta = 4$ and $\xi^2 = 0.1$. One can see a clear bump-like structure of the distribution, where the bump position coincides with the corresponding value of the carrier phase. The reason of such behaviour is the same as an alignment of the probability along $\phi_e = 0$ for $\tilde{\phi} = 0$ described in previous subsection. Indeed, now the basic functions Y_l and X_l are determined by the integral over $d\phi$ with a rapidly oscillating function proportional to the exponent

$$\mathrm{e}^{i\left[l\phi - z\left(\cos(\phi_e-\tilde{\phi})\int\limits_{-\infty}^{\phi} d\phi'\, f(\phi')\cos\phi' + \sin(\phi_e-\tilde{\phi})\int\limits_{-\infty}^{\phi} d\phi'\, f(\phi')\sin\phi'\right)\right]} . \tag{64}$$

Then, taking into account the inequality

$$\int\limits_{-\infty}^{\phi} d\phi'\, f(\phi')\cos\phi' \gg \int\limits_{-\infty}^{\phi} d\phi'\, f(\phi')\sin\phi' \ , \tag{65}$$

which is valid for the sub-cycle pulse with hyperbolic secant shape, one can conclude that the main contribution to the probability comes from the region $\phi_e \simeq \tilde{\phi}$, which is confirmed by the result of our full calculation shown in Fig. 20 (left panel).

The corresponding anisotropies defined by Eq. (58) are exhibited in Fig. 20 (right panel). One can see a strong dependence of the anisotropy on the carrier phase which leads to the

"bump" structure of the differential probabilities shown in the left panel. The anisotropy takes a maximum value $\mathcal{A} \simeq 1$ at $\phi_e = \tilde{\phi}$ and $|\mathcal{A}| < 1$ at $\phi_e \neq \tilde{\phi}$. It takes a minimum value $\mathcal{A} \simeq -1$ at $\phi_e - \tilde{\phi} = \pm\pi$.

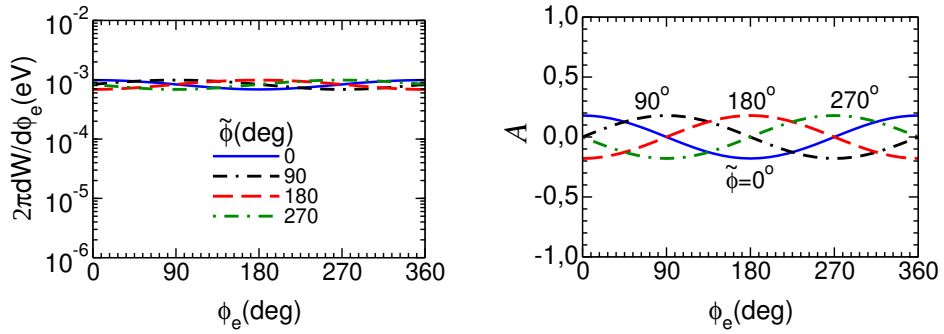

FIG. 21: The same as in Fig. 20 but for short pulse with $N = 2$.

The effect of the carrier phase decreases when the duration of pulse increases. Thus, when the number of oscillations in a pulse is $N \geq 2$, the inequality of two terms in (65) does not hold, instead they have the same order of magnitude and the alignment of the differential distributions with respect to $\phi_e \simeq \tilde{\phi}$ becomes very weak. The corresponding results are exhibited in Fig. 21. The probabilities (rates) $2\pi dW/d\phi_e$ as a function of ϕ_e for the short pulse with $N = 2$ and $\zeta = 4$ and $\xi^2 = 0.1$ for different $\tilde{\phi}$ are shown in the left panel. One can see a very weak dependence of the rates on ϕ_e and $\tilde{\phi}$. The rates are concentrated near the value $\sim 10^{-3}$ eV. Although, a small enhancement in the vicinity $\phi_e \simeq \tilde{\phi}$ still exists. This also is manifest in the anisotropy shown in the right panel. The anisotropy is finite, but its absolute value is less than 0.2.

In order to stress the alignment of the differential azimuthal-angle distributions along $\phi_e \simeq \tilde{\phi}$ one can plot differential distributions and anisotropies as a function of the "scale" variable $\Phi = \phi_e - \tilde{\phi}$. In this case, all curves shown, for example in the left and right panels in Fig. 20, are merged into a single carrier phase independent curve. The corresponding result is exhibited in Fig. 22, where one can see a carrier phase independence of the differential distributions and anisotropies shown in the left and right panels, respectively. Similarly, a carrier phase independent result is obtained for the short pulse with $N = 2$ shown in Fig. 23.

Formally, this follows from the fact that the carrier phase is included in the expressions for the basic functions (62) and (63) in the combination $\phi_e - \tilde{\phi}$. Therefore, the differential distributions are a function of $\Phi = \phi_e - \tilde{\phi}$ rather than of ϕ_e (for finite $\tilde{\phi}$). From the physical

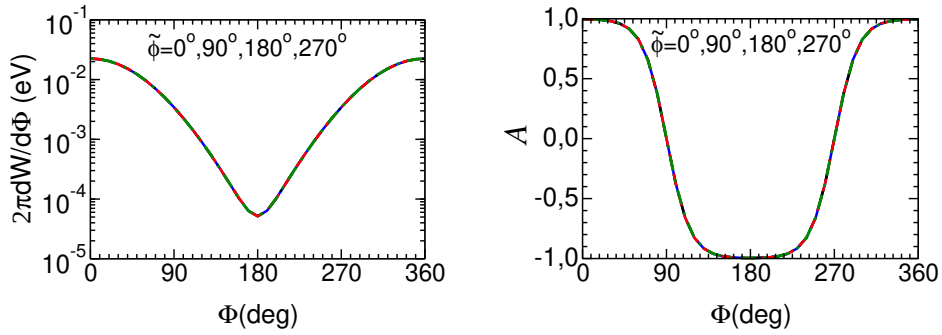

FIG. 22: The same as in Fig. 20 but as a function of the scale variable $\Phi = \phi_e - \tilde{\phi}$.

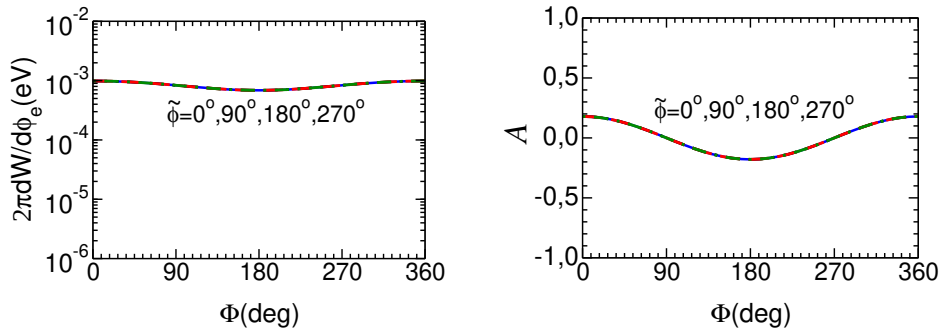

FIG. 23: The same as in Fig. 21 but as a function of the scale variable $\Phi = \phi_e - \tilde{\phi}$.

point of view this means that at finite $\tilde{\phi}$ the differential azimuthal distributions is convenient to study in the coordinates x', y' rotated relative to the initial coordinates x, y by an angle equal to the carrier phase $\tilde{\phi}$.

IV. COMPTON SCATTERING IN SHORT LASER PULSE

A. General formalism

The Compton scattering process is considered here as a spontaneous emission of one photon off an electron in an external e.m. field. Similarly to the Breit-Wheeler process, we employ the four-potential of a circularly polarized laser field in form of Eq. (1) with the envelope function $f(\phi)$ discussed in Sect. II. Here, we also use one-parameter hyperbolic secant (hs) envelope and two-parameter symmetrized Fermi (sF) shape with $b/\Delta = 0.15$. All details and notations are given in Sect. II. Using the same arguments as before, we start

our consideration assuming $\tilde{\phi} = 0$ and discuss the impact of the finite carrier phase later.

Utilizing the e.m. potential (1) and the Volkov solution for the electron wave function in this background field one finds to the following expression for the S matrix element

$$S = -ie \int_{-\infty}^{\infty} dl\, M(l) \frac{(2\pi)^4 \delta^4(p + lk - p' - k')}{\sqrt{2E\, 2E'\, 2\omega'}} \ , \tag{66}$$

where k, $k' = (\omega', \mathbf{k}')$, $p = (E, \mathbf{p})$ and $p' = (E', \mathbf{p}')$ refer to the four-momenta of the background (laser) field (1), scattered photon, as well as asymptotic incoming (in-state) and outgoing (out-state) electrons. All quantities are considered in the laboratory system. Similarly to the Breit-Wheeler process the transition matrix $M(l)$ consists of four terms (cf. Eq. (18)),

$$M(l) = \sum_{i=0}^{3} M^{(i)}\, C^{(i)}(l) \ , \tag{67}$$

where the transition operators have now the form $M^{(i)} = \bar{u}_{p'}\, \hat{M}^{(i)}\, u_p$ with

$$\begin{aligned} \hat{M}^{(0)} &= \not{\varepsilon}' \ , \quad \hat{M}^{(1)} = \frac{e^2 a^2\, (\varepsilon' \cdot k)\, \not{k}}{2(k \cdot p)(k \cdot p')} \ , \\ \hat{M}^{(2,3)} &= \frac{e \not{a}_{(1,2)} \not{k} \not{\varepsilon}'}{2(k \cdot p')} + \frac{e \not{\varepsilon}' \not{k} \not{a}_{(1,2)}}{2(k \cdot p)} \ . \end{aligned} \tag{68}$$

Here, u_p and $\bar{u}_{p'}$ are free Dirac spinors depending on the momenta p and p'; and ε' denotes the polarization four vector of the scattered photon. Since the Compton scattering is crossing channel of the Breit-Wheeler processes, the identity $\hat{M}^{(i)}_{\mathrm{Compton}}(p, p', k, k') = \hat{M}^{(i)}_{\mathrm{BW}}(-p, p', k, -k')$ is realized. Utilizing the prescription of Sect. 3. 1 one can express the coefficients $C^{(i)}(l)$ through basic functions $Y_l(z)$ and $X_l(z)$ (cf. Eqs. (28) and (29)) with

$$\mathcal{P}(\phi) = z \int_{-\infty}^{\phi} d\phi'\, \cos(\phi' - \phi_0) f(\phi') - \xi^2 \frac{u}{u_0} \int_{-\infty}^{\phi} d\phi'\, f^2(\phi') \tag{69}$$

and

$$z = 2l\xi \sqrt{\frac{u}{u_l}\left(1 - \frac{u}{u_l}\right)}, \ u \equiv (k' \cdot k)/(k \cdot p'), \ u_l = l/\, u_0 \ , \tag{70}$$

where $u_0 = 2k \cdot p/m^2$. Now, the phase ϕ_0 is equal to the azimuthal angle of the direction of flight of the outgoing electron, $\phi_0 = \phi_{e'}$, and it is related to the azimuthal angle of the momentum of the outgoing photon as $\phi_{\gamma'} = \phi_0 + \pi$.

This representation of functions $C^{(i)}(l)$ allows to define a partial differential cross section

$$\frac{d\sigma(l)}{d\omega'\, d\phi_{e'}} = \frac{2\alpha^2}{N_0\, \xi^2\, (s-m^2)\, |p - l\omega|}\, w(l) \tag{71}$$

with

$$\begin{aligned} w(l) \;&=\; -2\widetilde{Y}_l^2(z) + \xi^2(1 + \frac{u^2}{2(1+u)}) \\ &\times\; \Big(Y_{l-1}^2(z) + Y_{l+1}^2(z) - 2\widetilde{Y}_l(z) X_l^*(z)\Big)\;. \end{aligned} \tag{72}$$

Equation (72) resembles the corresponding expression for the partial probability of photon emission in the case of IPA [50] with the substitutions $l \to n = 1, 2, \cdots$ and $\widetilde{Y}_l^2(z)$, $Y_l^2(z)$, $\widetilde{Y}_l(z) X_l^*(z) \to J_n^2(z')$, namely

$$\begin{aligned} w_n \;&=\; -2J_n^2(z') + \xi^2(1 + \frac{u^2}{2(1+u)}) \\ &\times\; \big(J_{n-1}^2(z') + J_{n+1}^2(z') - 2J_n^2(z')\big)\;, \end{aligned} \tag{73}$$

where $J_n(z')$ denotes Bessel functions with $z' = \frac{2n\xi}{\sqrt{1+\xi^2}} \sqrt{\frac{u}{u_n}\left(1 - \frac{u}{u_n}\right)}$ and $u_n = \frac{2n(k\cdot p)}{m^2(1+\xi^2)}$. Similarly to IPA, the phase ϕ_0 can be determined through invariants $\alpha_{1,2}$ as $\cos\phi_0 = \alpha_1/z$, $\sin\phi_0 = \alpha_2/z$ with $\alpha_{1,2} = e\,(a_{1,2}\cdot p/k\cdot p - a_{1,2}\cdot p'/k\cdot p')$. The dimensionless field intensity ξ^2 is described by Eqs. (2) - (6).

The frequency ω' of the emitted photon is related to the auxiliary variable l and the polar angle θ' of the direction of the momentum $\mathbf{k}'$ via

$$\omega' = \frac{l\,\omega(E + |\mathbf{p}|)}{E + |\mathbf{p}|\cos\theta' + l\omega(1 - \cos\theta')} \tag{74}$$

and increases with l at fixed θ' since ω' is a function of l at fixed θ'. For convenience, we also present a similar expression for IPA, where the fermions are dressed and the integer quantity n, together with the field intensity ξ^2, appear:

$$\omega' = \frac{n\,\omega(E + |\mathbf{p}|)}{E + |\mathbf{p}|\cos\theta' + \omega(n + \frac{m^2\xi^2}{2(k\cdot p)})(1 - \cos\theta')}\;. \tag{75}$$

The differential cross section of the one-photon production is eventually

$$\frac{d\sigma}{d\omega'} = \int\limits_{\eta} dl \int\limits_{0}^{2\pi} d\phi_{e'} \frac{d\sigma(l)}{d\omega' d\phi_{e'}} \delta\left(l - l(\omega')\right)\;. \tag{76}$$

The lower integration limit $\eta > 0$ is defined by kinematics, i.e. by the minimum value of the considered ω', in accordance with Eq. (74). In the IPA case, the variable $n = 1, 2, \cdots$ refers

to the contribution of the individual harmonics ($n = 1$ with $\xi^2 \ll 1$ recovers the Klein-Nishina cross section, cf. [17]). The value $n\omega$ is related to the energy of the background field involved in Compton scattering. Obviously, this value is a multiple of ω. In FPA, the internal quantity l is a continuous variable, implying a continuous distribution of the differential cross section over the $\omega' - \theta'$ plane. The quantity $l\omega$ can be considered as energy of the laser beam involved in the Compton process, which is not a multiple ω. Mindful of this fact, without loss of generality, we denote the processes with $l > 1$ as a multi-photon generalized Compton scattering, remembering that l is a continuous quantity.

The multi-photon effects become most clearly evident in the partially energy-integrated cross section

$$\tilde{\sigma}(\omega') = \int\limits_{\omega'}^{\infty} d\bar{\omega}' \frac{d\sigma(\bar{\omega}')}{d\bar{\omega}'} = \int\limits_{l'}^{\infty} dl \frac{d\sigma(l)}{dl} \ , \tag{77}$$

where $d\sigma(l)/dl = (d\sigma(\omega')/d\omega')(d\omega'(l)/dl)$, and the minimum value of l' is

$$l' = \frac{\omega'}{\omega} \frac{E + |\mathbf{p}| \cos\theta'}{E + |\mathbf{p}| - \omega'(1 - \cos\theta')} \ . \tag{78}$$

The cross section (77) has the meaning of a cumulative distribution. In this case, the subthreshold, multi-photon events correspond to frequencies ω' of the outgoing photon which exceed the corresponding threshold value $\omega'_1 = \omega'(l = 1)$ (cf. Eq. (74)), and ratio $\kappa = \omega'/\omega'_1 > 1$ represents the sub-threshold parameter.

B. The differential cross section

In IPA [17, 50], the cross section of the multi-photon Compton scattering increases with θ' towards 180^o. For instance, it peaks at about 170^o for the chosen electron energy of 4 MeV (all quantities are considered in the laboratory frame) and rapidly drops to zero when θ' approaches 180^o for the harmonics $n > 1$ yielding thus the blind spot for back-scattering. Therefore, in our subsequent analysis we choose the near-backward photon production at $\theta' = 170^o$ and an optical laser with $\omega = 1.55$ eV. Defining one-photon events by $n = 1$, this kinematics leads via Eq. (75) to $\omega'_1 \equiv \omega'(n = 1, \xi^2 \ll 1, \theta' = 170^o) \simeq 0.133$ keV which we refer to as a threshold value. Accordingly, $\omega' > \omega'_1$ is enabled by non-linear effects, which in turn may be related loosely to multi-photon dynamics with $n > 1$ in IPA or $l > 1$ in FPA where, we remind again, the internal variable l can not be interpreted strictly as number

of laser photons involved (cf. [52]). Note that all calculations for IPA are performed in a standard way [17, 50]. The energy of the outgoing photon in IPA is calculated using Eq. (75), where dressing of electrons in the background field is taken into account.

Let us consider first an example of short pulses with moderate intensity, $\xi^2 = 10^{-3}$, similar to a recent experiment of Compton backscattering [53]. Results for the hs and sF shapes are exhibited in Fig. 24. The solid and the dashed curves correspond to pulses with $N = 2$ and 5, respectively. The stars depict the IPA results, i.e., the harmonics at fixed scattering angle θ'. Their positions correspond to integer values of $n = 1, 2, \cdots$ in accordance with Eq. (75). i.e. the distribution of scattered photon energies is a discrete function of ω'. We stress that the cross section at $\omega' > \omega'_1$ is essentially "sub-threshold" , i.e. outside the kinematically allowed region of the Klein-Nishina process due to multi-photon effects.

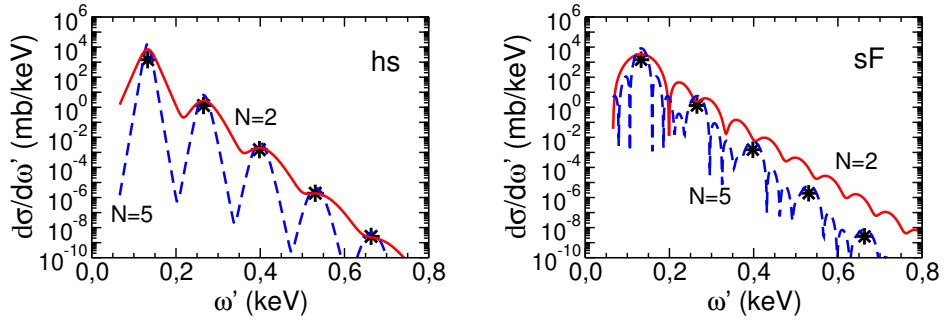

FIG. 24: Differential cross section $d\sigma/d\omega'\,|_{\theta'=170^o}$ of the Compton scattering for $\xi^2 = 10^{-3}$. The solid and dashed curves are for $N = 2$ and 5, respectively. The stars depict the IPA results for lowest harmonics. Left and right panels correspond to hyperbolic secant (hs) and symmetrized Fermi (sF) shapes of the envelopes, respectively.

In the FPA case, the energy distribution becomes a continues function of ω'. The actual shape is determined by both the pulse duration and the envelope form. Consider first the case of the hs shape (cf. Fig. 24, left panel). The cross section displays sharp bumps with peak positions corresponding to integer values of $l = n$ (as in IPA). In the vicinity of the bumps, at $l = n \pm \epsilon$, $\epsilon \ll 1$, the cross section is rapidly decreasing. Such a behavior reflects the properties of the functions $Y_{l=n+\epsilon}(z)$ (cf. Eq. (37)) which is proportional to the Fourier transform of the $(n + 1)$-th degree of the envelope function $F^{(n+1)}(\epsilon)$. At $\xi^2 \ll 1$, the contribution of terms $\propto X_l$ is negligible.

The behavior of the cross section in the vicinity of the first bump is proportional to

$F^2_{\rm hs}(\epsilon)$ with $F_{\rm hs}(\epsilon)$ given in Eq. (38), or $F_{\rm hs}(x) \simeq \Delta \exp[-\pi\Delta x/2]$. Thus, the cross section becomes steeper with increasing pulse duration Δ. This result qualitatively agrees with that of Ref. [23].

In the case of the sF shape, the dependence $F_{\rm sF}(\epsilon)$ is more complicated (cf. Eq. (38)). Together with the overall decrease of the cross section proportional to $\exp[-2\pi b\, l(\omega')]$ it also indicates fast oscillations with a frequency $\propto \Delta$. Such oscillations show up in the cross section as some secondary bumpy structures. These properties are manifest in Fig. 24 (right panel): the overall decrease of the cross section decreases with decreasing pulse duration, and the number of the secondary bumps in the region of ω', corresponding to the nearest integer values of l, increases with pulse duration.

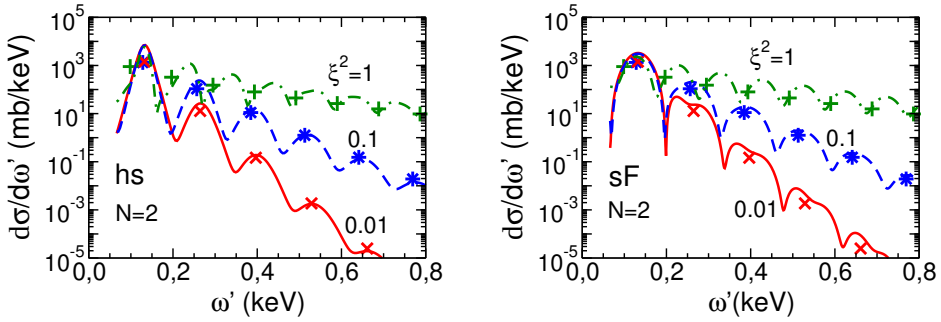

FIG. 25: Differential cross section $d\sigma/d\omega'\,|_{\theta'=170^o}$ of the Compton scattering for $\xi^2 = 0.01$, 0.1 and 1, shown by solid, dashed, and dot-dashed curves, respectively, for $N = 2$. The symbols "x" , stars and pluses depict the IPA results for the lowest harmonics for $\xi^2 = 0.01$, 0.1, and 1, respectively. Left and right panels correspond to hyperbolic secant (hs) and symmetrized Fermi (sF) shapes of the envelopes.

In Fig. 25 we present the differential cross sections for different field intensities $\xi^2 =$ 0.01, 0.1 and 1, depicted by solid, dashed, and dot-dashed curves, respectively. The duration of the pulse corresponds to $N = 2$. The bump positions for FPA in Fig. 25 are shifted relative to the discrete positions of contributions from the individual harmonics in IPA, shown by corresponding symbols. These shifts are a consequence of the electron dressing in IPA which depends on ξ^2.

For completeness, in Fig. 26 we exhibit the differential cross sections for a sub-cycle pulse with $N = 0.5$ for $\xi^2 = 10^{-3}$ and 1, shown by solid and dot-dashed curves, respectively, for the hs (left) and sF (right) envelope shapes. Crosses and pluses depict the IPA results for

$\xi^2 = 10^{-3}$, and 1. For the hs shape, the cross sections decrease almost monotonically, with

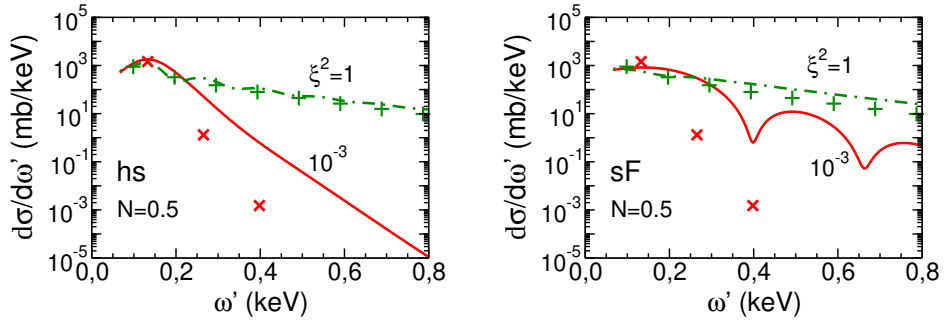

FIG. 26: Differential cross section $d\sigma/d\omega'\,|_{\theta'=170^o}$ of Compton scattering for $\xi^2 = 10^{-3}$ and 1 shown by solid and dot-dashed curves, respectively, for $N = 0.5$. Crosses and pluses depict the discrete IPA results for lowest harmonics for $\xi^2 = 10^{-3}$ and 1, respectively. Left and right panels correspond to hyperbolic secant (hs) and symmetrized Fermi (sF) envelope shapes.

a large enhancement of the FPA result compared to IPA for small field intensities ($\xi^2 \ll 1$). In the case of the flat-top envelope the cross section exhibits some oscillations which point to more complicated spectral properties of the flat-top envelope shape.

To summarize this part we can conclude that the results for fully differential cross sections for IPA and FPA are quite different. In IPA, the cross section represents the discrete spectrum where the frequencies of the outgoing photons ω' are fixed according to Eq. (75). In FPA, the differential cross sections are continuous functions of ω'. Some similarities of IPA and FPA can be seen in the case of small field intensities $\xi^2 \ll 1$ and the smooth one-parameter envelope shape with $N = 2 \ldots 10$. Here, the differential cross sections have a bump structure, where the position of bumps and bump heights are close to that of IPA. The situation changes drastically for more complicated (and probably more realistic) flat-top envelope shapes. In this case one can see a lot of additional bumps which reflect the more complicated spectral properties of the flat-top shape; it is difficult to find a relation not only between IPA and FPA, but also within FPA for different pulse durations. Experimentally, studying multi-photon effects using rapidly oscillating fully differential cross sections seems to be rather complicated. An analysis of integral observables helps to overcome this problem. In particular, the partially integrated cross sections have a distinct advantage: they are smooth functions of ω' and allow to study directly the multi-photon dynamics.

C. Partially integrated cross sections

The non-linear dynamics becomes most transparent in the partially energy-integrated cross section defined in Eq. (77). In this case, the sub-threshold multi-photon events are filtered when the lower limit of integration ω' exceeds the threshold value $\omega'_1 = \omega'(n = 1, \xi^2)$ (with $\xi^2 \ll 1$ for the pure Klein-Nishina process). Thus, events with $\omega'(l) \gg \omega'_1$ and $l \gg 1$ correspond essentially to multi-photon process, where the energy $l\omega \gg \omega$ is absorbed from the pulse. Experimentally, this can be realized by an absorptive medium which is transparent for frequencies above a certain threshold ω'. Otherwise, such a partially integrated spectrum can be synthesized from a completely measured spectrum. Admittedly, the considered range of energies with a spectral distribution uncovering many decades is experimentally challenging.

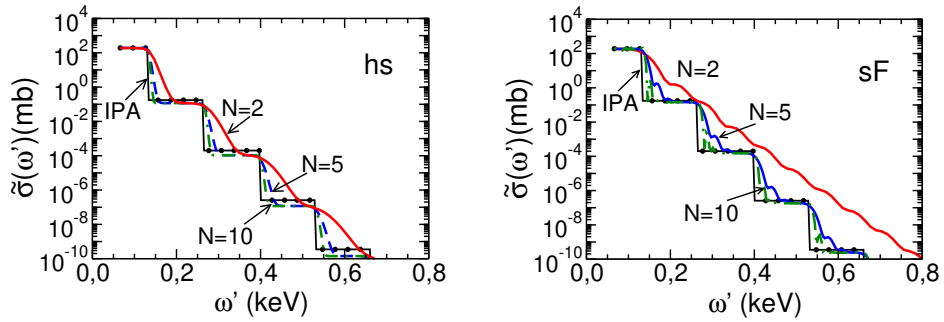

FIG. 27: The partially integrated cross section (77) for $\xi^2 = 10^{-3}$. The thin solid curve marked by dots depicts the IPA result. The solid, dashed, and dot-dashed curves correspond to $N = 2$, 5 and 10, respectively. Left and right panels are for hyperbolic secant (hs) and symmetrized Fermi (sF) envelopes.

The partially integrated cross sections of Eq. (77) are presented in Fig. 27. The thin solid curve (marked by dots) depicts IPA results given by

$$\tilde{\sigma}^{IPA}(\omega') = \int\limits_{l'(\omega')}^{\infty} dl \sum_{n=1}^{\infty} \frac{d\sigma_n^{IPA}}{d\omega'_n} \frac{d\omega'_n}{dn} \theta(n-l) \ , \tag{79}$$

where $\omega'(n)$ is defined by Eq. (75). That is, the partially integrated cross section becomes a step-like function, where each new step corresponds to the contribution of a new (higher) harmonic n, which can be interpreted as n-laser photon process. Results for the finite

pulse exhibited by solid, dashed, and dot-dashed curves correspond to $N = 2$, 5 and 10, respectively. In the above-threshold region with $\omega' \leq \omega'_1$, the cross sections do not depend on the widths and shapes of the envelopes, and the results of IPA and FPA coincide. The situation changes significantly in the deep sub-threshold region, where $\omega' > \omega'_1$ ($l \gg 1$), $n \gg 1$. For short pulses with $N \simeq 2$, the FPA results exceed that of IPA considerably, and the excess may reach several orders of magnitude, especially for the flat-top envelope shown by the solid curve in Fig. 27 (right panel). However, when the number of oscillation in a pulse increases ($N \gtrsim 10$) there is a qualitative convergence of FPA and IPA results, independently of the pulse shape. Thus, at $N = 10$ and $\omega' = 0.6$ keV the difference between predictions for hs and sF shapes is a factor of two, as compared with the difference of the few orders of magnitude at $N = 2$ for the same value of ω'.

To highlight the difference of the hs and sF (flat-top) shapes for short pulse we exhibit in Fig. 28 (left panel) results for $N = 2$. At $\omega' \gtrsim 0.6$ keV, the difference between them is more than two orders of magnitude.

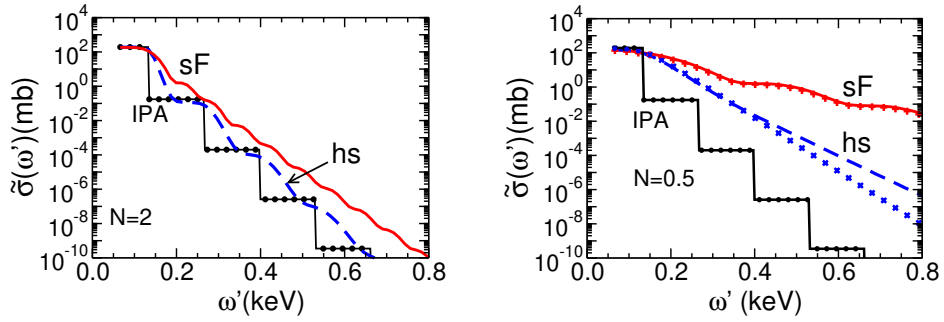

FIG. 28: The partially integrated cross section (77) for $\xi^2 = 10^{-3}$. Left panel: $N = 2$, for the hyperbolic secant (hs, dashed curve) and symmetrized Fermi (sF, solid curve) shapes. Right panel: The same as in left panel, but for a sub-cycle pulse with $N = 0.5$. The crosses and pluses correspond to the asymptotic solutions for hs and sF shapes, respectively, described in the text.

Consider now the case of sub-cycle pulses with $N < 1$. Our result for $N = 0.5$ is exhibited in Fig. 28 (left panel). One can see a large enhancement of the cross section with respect to the IPA case for the sub-cycle pulse in the sub-threshold region. The enhancement for the sF shape is much greater pointing to a sensible dependence on the actual pulse shape. For a qualitative estimate of such a behavior we can drop the $\phi_{e'}$ dependence by taking $\phi_{e'} = 0$. This choice is quite reasonable for the flat-top sF envelope shape and may serve

as an upper limit for the cross sections in the case of the smooth hs envelope shape. Under the considered conditions the basic function Y_l in Eq. (28) can be approximated as

$$\begin{aligned} Y_l &\simeq \frac{1}{2\pi}\mathrm{e}^{-il\phi_0}\int dq\, F(q)\int d\phi \mathrm{e}^{i(l-q)\phi - i\mathcal{P}(\phi)} \\ &\simeq \frac{1}{2\pi}\int dq\, F(q)\int d\phi \mathrm{e}^{i(l-q-l\beta\xi)\phi - i\delta} = \mathrm{e}^{-i\delta}F(\tilde{l}) \ , \end{aligned} \tag{80}$$

where $F(l)$ is the Fourier transform of the envelope function, $\tilde{l} = l(1-\beta\xi)$ with $\beta = 2\sqrt{\frac{u}{u_l}(1-\frac{u}{u_l})} < 1$ and $\delta = z\int_{-\infty}^{0} d\phi \cos\phi\, f(\phi) - l\phi_0$. As a result, the cross section is almost completely defined by the square of the Fourier transforms (cf. Eqs. (38)), i.e. $\tilde{\sigma}(\omega') \simeq g(l(\omega'))\, F^2(\tilde{l}(\omega') - 1)$, where $g(\omega')$ is a smooth function of $l = l(\omega')$ (cf. Eq. (86)). The Fourier transform for the sF shape decreases slower with increasing l. Such a dependence is evident in Fig. 27 (right panel). For an illustration, the crosses depict the result of a calculation where the basic functions Y_l and X_l in the partial probability $\omega'(l)$ in Eq. (72) are replaced by their asymptotic values $F^{(1)}(\tilde{l}-1)$ and $F^{(2)}(\tilde{l}-1)$, respectively. A more detail discussion of the asymptotic result is presented below (cf. Eq. (86)).

The dependence of the partially integrated cross section as a function of ξ^2 at fixed ratio $\kappa \equiv \omega'/\omega'_1 = 3$ for short pulses with $N = 0.5$ and 2 is exhibited in Fig. 29 in left and right panels, respectively. Note that the minimum value of $l'(\omega')$ is related to κ as

$$l'(\omega') \ = \ \kappa\frac{E + |\mathbf{p}|\cos\theta'}{E + |\mathbf{p}|\cos\theta' + \omega(1-\kappa)(1-\cos\theta')} \ , \tag{81}$$

meaning $l' < \kappa$. Similarly, for $n_{\min}$ one has $n_{\min} = x$, for $I(x) = x$ and $n_{\min} = x+1$ for $I(x) < x$ with

$$x = \frac{E + |\mathbf{p}|\cos\theta' + \frac{\omega m^2\xi^2}{2(k\cdot p)}(1-\cos\theta')}{E + |\mathbf{p}|\cos\theta' + \omega(1-\kappa+\frac{m^2\xi^2}{2(k\cdot p)})(1-\cos\theta')}. \tag{82}$$

The solid curves and symbols correspond to IPA and FPA, respectively, with different pulse shapes. One can see that the main difference of IPA and FPA, as well as the pulse shape dependence, appears at small field intensities $\xi^2 \ll 1$, where the dependence of the cross section on the pulse shape and duration is essential.

To explain this result we use the asymptotic solution for $\tilde{\sigma}$ which is obtained by keeping leading terms in ξ^2 in Eqs. (72) and (73) and taking into account that the dominant contribution to the integrals of Eqs. (77) and (79) stems from $l \sim l'$ and $n \sim I(l')+1$, respectively. Consider first the partially integrated cross section in IPA. Using the asymptotic expression

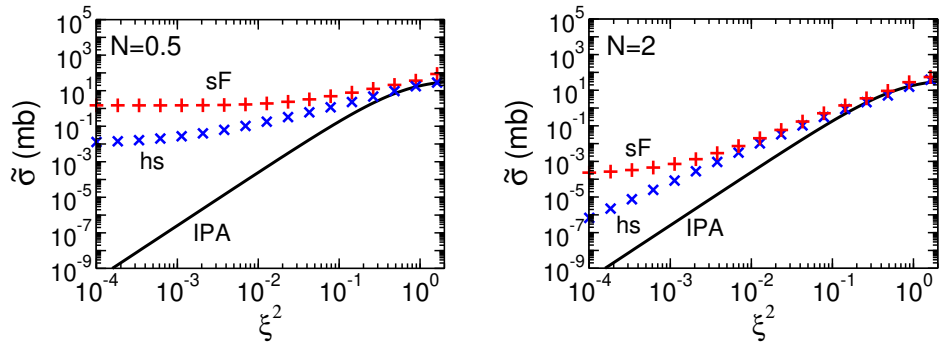

FIG. 29: The partially integrated cross section as a function of ξ^2 at $\kappa = \omega'/\omega'_1 = 3$ for short pulses with $N = 0.5$ (left) and 2 (right). The solid curve and symbols correspond to IPA and FPA (hs and sF envelope functions), respectively.

for the Bessel functions

$$J_k(z) \simeq \left(\frac{z}{2}\right)^k \frac{1}{k!} \quad \text{for} \;\; z \ll 1 \;, \tag{83}$$

and keeping the leading terms in Eq. (73) with $J^2_{n-1}(z)$ and $n = I(l') + 1$, one obtains

$$\tilde{\sigma}^{IPA} \simeq \frac{2\pi\alpha^2}{(E + |\mathbf{p}|\cos\theta')|\mathbf{p}|}\xi^{2k}\Phi(k) \;, \tag{84}$$

where $k = I(l') \simeq I(\kappa)$ and

$$\begin{aligned} \Phi(k) \;&=\; \frac{(k+1)^{2(k+1)}}{(k+1)!^2}\left(t_k(1-t_k)\right)^{2k} \\ &\times\; \left(1 + \frac{u}{2(1+u)} - 2t_k(1-t_k)\right) \end{aligned} \tag{85}$$

with $t_k = u/u_k$, where $u = \omega'(1-\cos\theta')/(E+|\mathbf{p}|-\omega'(1-\cos\theta'))$ and $u_k = 2k\omega(E+|\mathbf{p}|)/m^2$. Within the considered kinematics, t_k does not depend on k and can be approximated by $t_k \simeq m^2(1-\cos\theta')/(2(E+|p|\cos\theta')(E+|p|)) \simeq 0.35$.

The result for the asymptotic solution for IPA of (84) is shown by the solid black curve in Fig. 30 together with a full calculation depicted by stars. One can see an excellent agreement of these two results.

For FPA, in the case of sub-cycle pulse with $N = 0.5$, we use the asymptotic representation for the basic functions Y_l in the form of Eq. (80) which allows to express the partially integrated cross section as

$$\tilde{\sigma} \simeq \frac{2\pi\alpha^2}{N_0(E + |\mathbf{p}|\cos\theta')|\mathbf{p}|}$$

$$\times \left(1+\frac{u}{2(1+u)}-2t_{l'}(1-t_{l'})\right)\int_{l'}^{l'+1} dl\, F^2(\tilde{l}-1)\ , \tag{86}$$

where $F(x)$ is the Fourier transform of the envelope function (cf. Eq. (38)). Results for the

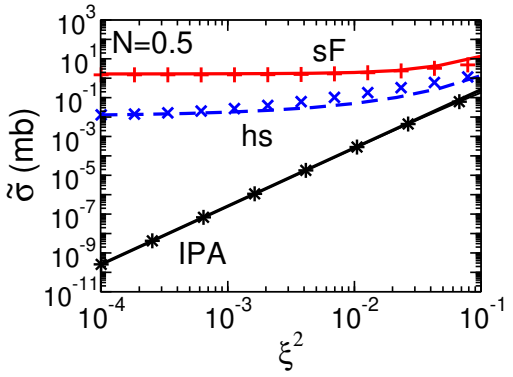

FIG. 30: The partially integrated cross sections as a function of $\xi^2 \ll 1$ for a sub-cycle pulse with $N = 0.5$. The stars are for the full IPA result. The thick solid curve corresponds to the asymptotic solution of Eq. (84). The pluses and crosses are for full calculations for sF and hs shapes, respectively, while the dashed and dot-dashed curves are the corresponding asymptotic results of Eq. (86).

sub-cycle pulse with $N = 0.5$ are presented in Fig. 30, where the pluses and crosses are for full calculations for the sF and hs shapes, respectively. The dashed and dot-dashed curves are the asymptotic solution of Eq. (86) for sF and hs shapes, respectively.

We would like to note that, at $\xi^2 \ll 1$, our asymptotic solution for sub-cycle pulse weakly depends on ξ only through the weak $l(1-\beta\xi)$ dependence in the Fourier transform. The leading ξ^2 dependence of the partial harmonics w_l in (72) is compensated by the ξ^2 dependence of the flux factor in the denominator of Eq. (71). Nevertheless, such a weak ξ dependence is in qualitative agreement of full and asymptotic solutions, both for sF and hs envelope shapes. Thus, we can conclude that the partially integrated cross section for the sub-cycle pulse at $\xi^2 \ll 1$ is almost completely determined by the square of the Fourier transform of the envelope function which is a measure of high momentum frequencies generated by the pulse shape.

In the case of a short pulse with $N = 2$ and $\xi^2 \leq 0.1$, we use for the asymptotic solution

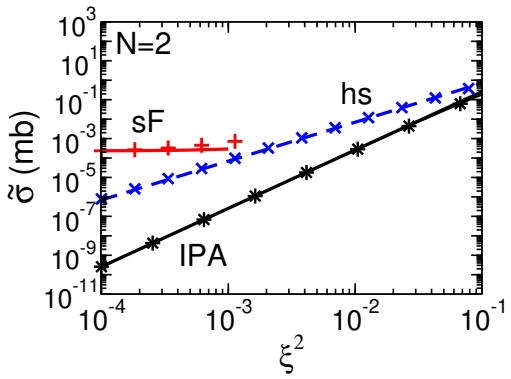

FIG. 31: Results for a short pulse with $N = 2$. The symbols stars, pluses and crosses are full calculations, for IPA and FPA for sF and hs shapes, respectively; the solid black, dashed, and dot-dashed curves are the corresponding asymptotic results of Eqs. (84), (86) and (88), respectively.

asymptotic expression of the basic functions of Eq. (37). Note that such an expression is valid only for the smooth one-parameter envelope shapes, where the function $\mathcal{P}(\phi)$, defined in Eq. (28), takes a simple form $\mathcal{P}(\phi) = z\sin(\phi - \phi_0)f(\phi) + \mathcal{O}(\xi^2)$ (cf. Eq. (34)). One can see that, if the argument obeys $l' > I(l')$, then the main contribution to the cross section comes from the two terms with

$$Y_{k,\varepsilon_1}(z) \quad \text{and} \quad Y_{k+1,\varepsilon_2}(z) \ , \tag{87}$$

where $k = I(l')$, $\varepsilon_1 = l' - I(l') \equiv \varepsilon > 0$, and $\varepsilon_2 = \varepsilon - 1 < 0$. Then, keeping the leading terms in ξ^2 in (72) one can get an approximate expression for the partially integrated cross section in the form

$$\begin{aligned} \tilde{\sigma} \simeq & \frac{2\pi\alpha^2}{N_0(E + |\mathbf{p}|\cos\theta')|\mathbf{p}|}\xi^{2(k-1)} \\ \times & \left(\Phi(k-1) \int_{\varepsilon}^{1} d\epsilon \, (F^{(k)}(\epsilon))^2 \right. \\ & \left. + \xi^2 \, \Phi(k) \int_{\varepsilon-1}^{1} d\epsilon (F^{(k+1)}(\epsilon))^2 \right) \ , \end{aligned} \tag{88}$$

where $F^{(m)}$ is the Fourier transform of m-th power of the envelope function $f(\phi)$. The full and approximate results for $\tilde{\sigma}$ are shown in Fig. 31 by crosses and the dot-dashed thick

curve, respectively. One can see a fairly good agreement of approximate and full results up to $\xi^2 = 0.1$.

In the case of the flat-top envelope, the integrand of $\tilde{\sigma}$ has a more complicated structure with a large number of bumps. The asymptotic solution for the basic functions of Eq. (37) does not apply here. However, as a first approximation one can use the asymptotic solution of Eq. (80). Then, the cross section $\tilde{\sigma}$ is determined by Eq. (86). The full and approximate results for $\tilde{\sigma}$ are shown in Fig. 31 by pluses and the dashed curve, respectively. One can see an agreement of full and approximated results, however, in a very limited range of $\xi^2 \ll 1$.

To summarize this part we note that, in the case of short pulses and small field intensities, the partially integrated cross section is determined by the interplay of pulse shape and multiphoton dynamics. For both considered shapes, the cross sections are described by the simple asymptotic expressions which can be used in practical research.

At large values $\xi^2 \gg 1$, our analysis shows that the dependence on the envelope shape disappears because, similar to the Breit-Wheeler process, only the central part of the envelope becomes important. Formally, under a change of the variable $l \to l_{\text{eff}} = l + m^2\xi^2 u/2(k \cdot p)$, the basic functions $Y_l(z)$ with $l \gg 1$, $z \gg 1$ become similar to the asymptotic form of the Bessel functions $J_l(z)$ and, as a consequence, one can get the total production probability (or the total cross section) in the form of IPA[17] with a slightly modified pre-exponential factor.

D. Effect of the finite carrier phase

The generalization of our approach to the case of the finite carrier phase $\tilde{\phi}$ in e.m. potential (1) is carried out by the same method as in the case of e^+e^- pair production described in Sect. 3. 7. The functions $C^{(i)}(l)$ in transition matrix (67) are transformed according to Eq. (60) with

$$\mathcal{P}(\phi) = z \int_{-\infty}^{\phi} d\phi' \, \cos(\phi' - \phi_0 + \tilde{\phi}) f(\phi') - \xi^2 \frac{u}{u_0} \int_{-\infty}^{\phi} d\phi' \, f^2(\phi') \, , \tag{89}$$

where the variables z, u and u_0 are defined in (70). Then, using the basic functions $Y_l(z)$ and $X_l(z)$ in the form of Eq. (62) and utilizing Eq. (63) one can obtain the partial differential cross section $d\sigma(l)/d\omega' d\phi_{e'}$ in the form of Eq. (71) with $w(l)$ given by Eq. (72), but with new basic functions Y_l and X_l which now depend on carrier phase $\tilde{\phi}$ according to Eq. (62)

with (89). Recall, that $\phi_0 = \phi_{e'}$ is the azimuthal angle of the outgoing electron momentum. The differential partially integrated cross section reads

$$\frac{d\tilde{\sigma}(\omega')}{d\phi_{e'}} = \int\limits_{\omega'}^{\infty} d\bar{\omega}' \frac{d\sigma(\bar{\omega}')}{d\bar{\omega}'\, d\phi_{e'}} \ . \tag{90}$$

It is natural to expect that the effect of the finite carrier phase essentially appears in the differential cross section of the generalized Compton scattering as a function of the azimuthal angle of the outgoing electron momentum because the carrier phase is included in the expressions for the basic functions (62) in the combination $\phi_{e'} - \tilde{\phi}$.

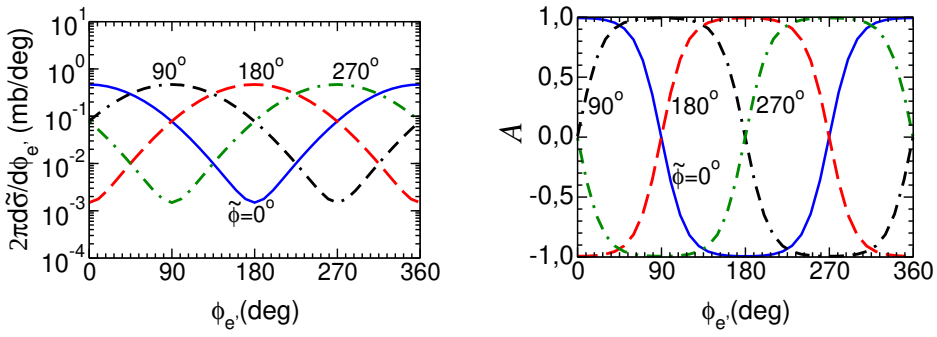

FIG. 32: Left panel: The differential cross section (90) as a function of the azimuthal angle of the outgoing electron momentum $\phi_{e'}$ for different values of the carrier phase $\tilde{\phi}$. The solid, dash-dash-dotted, dashed and dash-dotted curves correspond to the carrier phase equal 0, 90, 180 and 270 degrees, respectively. Right panel: The anisotropy (58) as a function of $\phi_{e'}$ for different $\tilde{\phi}$. For the hyperbolic secant shape with $N = 0.5$; $\xi^2 = 0.1$ and $\kappa = \omega'/\omega'_1 = 4$.

As an example, in Fig. 32 (left panel) we show the differential cross section (90) as a function of the azimuthal angle $\phi_{e'}$ for different values of the carrier phase $\tilde{\phi}$ for the sub-cycle pulse with $N = 0.5$ for the hyperbolic secant shape with $\kappa = \omega'/\omega'_1 = 4$ and $\xi^2 = 0.1$. One can see a clear bump-like structure of the distribution, where the bump position coincides with the corresponding value of the carrier phase. The reason of such behaviour is the same as an alignment of the probability along $\phi_e = \tilde{\phi}$, described in Sect. 3. 7. Corresponding anisotropies defined as

$$\mathcal{A} = \frac{d\tilde{\sigma}(\phi_{e'}) - d\tilde{\sigma}(\phi_{e'} + \pi)}{d\tilde{\sigma}(\phi_{e'}) + d\tilde{\sigma}(\phi_{e'} + \pi)} \tag{91}$$

are exhibited in Fig. 32 (right panel). One can see a strong dependence of the anisotropy on the carrier phase which follows to the bump-like behavior of the differential probabilities

shown in the left panel. Similar to the Breit-Wheeler process, the anisotropy takes a maximum value $\mathcal{A} \simeq 1$ at $\phi_{e'} = \tilde{\phi}$ and $|\mathcal{A}| < 1$ at $\phi_{e'} \neq \tilde{\phi}$. It takes a minimum value $\mathcal{A} \simeq -1$ at $\phi_e - \tilde{\phi} = \pm\pi$.

The differential cross sections and anisotropies as functions of the "scale" variable $\Phi = \phi_{e'} - \tilde{\phi}$ at fixed values of $\tilde{\phi}$ are exhibited in Fig. 33 in the left and right panels, respectively. All curves shown, in the left and right panels in Fig. 33, are merged into a single carrier phase independent curve. Similar to the Breit-Wheeler process, such a carrier phase independence

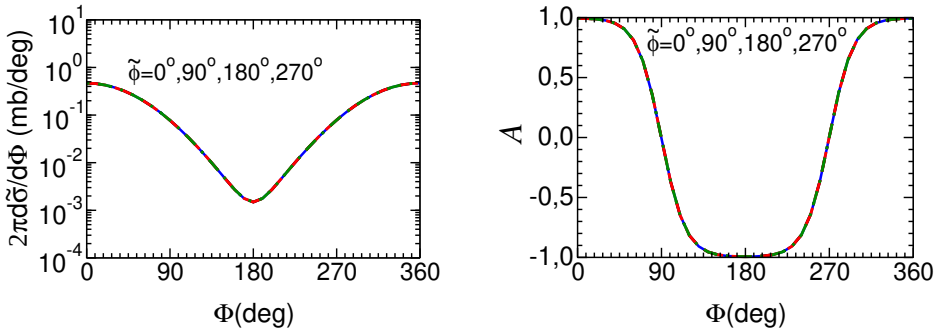

FIG. 33: The same as in Fig. 32 but as a function of the scale variable $\Phi = \phi_{e'} - \tilde{\phi}$.

of the differential cross sections and anisotropies is a consequence of the $\phi_0 - \tilde{\phi} = \phi_{e'} - \tilde{\phi}$ dependence of the basic functions in Eqs. (62) and (63).

The effect of the carrier phase decreases with increasing pulse duration. Taking into account the similarity between Breit-Wheeler and Compton scattering processes we do not show here the result for the Compton scattering (for $N \geq 2$), limiting to the most striking example of sub-cycle pulse, exhibited in Figs. 32 and 33.

V. SUMMARY

In summary we have considered two elementary quantum processes occurring in a short and intense electromagnetic (laser) pulses. They are the e^+e^- pair production (generalized Breit-Wheeler process) and the crossed process i.e. emission of single photon off an electron (generalized Compton scattering). We emphasized the very significant impact of the temporal pulse structure. Still, the pulses are approximated by plane waves, meaning that curved wave fronts deserve in future also dedicated investigations.

The pair production in the sub-threshold region with $\zeta > 1$ is currently a subject of

great interest. We have shown that the production probability is determined by a non-trivial interplay of two dynamic effects. The first one is related to the shape and duration of the pulse. The second one is the non-linear dynamics of charged particles in the strong electromagnetic field itself, independently of the pulse geometry. These two effects play quite different roles in two limiting cases. The pulse shape effects are manifested clearly at small values of product the $\xi\zeta$, where ξ characterizes the laser intensity and ζ refers to the threshold kinematics. The rapid variation of the e.m. field in a very short pulse amplifies the multi-photon events, and moreover, the probability of multi-photon events in the finite pulse approximation (FPA) can exceed the prediction of the infinite pulse approximation (IPA) by orders of magnitude. Thus, for example in the case of an ultra-short (sub cycle) pulse with the "number of oscillations" N in the pulse less than one, the production probability as a function of ζ is almost completely determined by the square of the Fourier transform of the pulse envelope function. High-l components, where l is the Fourier conjugate to the invariant phase variable ϕ, lead to the enhancement of the production probability. Among the considered envelope shapes, the flat-top shape with fast ramping and deramping intervals is most promising to obtain the highest probability. We also find that the different envelope shapes lead to anisotropies of the electron (positron) emission which can be studied experimentally. For short pulses with $N < 10$, the effects of the pulse shape are also important and the final yield differs significantly from the IPA prediction. This difference depends on the envelope shapes and the pulse duration.

Contrary to that, the non-linear multi-photon dynamics of e^+e^- production in a strong electromagnetic field plays a crutial role at large field intensities, $\xi^2 \gg 1$. Here, the effects of the pulse shape and duration disappear since the dominant contribution comes from the central part of the envelope function. As a result, the probabilities in FPA and IPA coincide.

In the transition region of intermediate intensities $\xi^2 \sim 1$, the probability is determined by the complex interplay of the both effects, and they must be taken into account simultaneously by a direct numerical evaluation of the multi-dimensional integrals with rapidly oscillating integrands.

The effect of the carrier phase manifests itself most clearly in ultra short (sub-cycle) pulses in azimuthal distributions of direction of flight of the outgoing electron (positron). The production probability has a bump-like structure where the bump position coincides with the value of carrier phase. This leads to a definite alignment of the differential cross

section and anisotropy in the $x-y$ plane along the angle equal to the carrier phase. The impact of the carrier phase decreases with increasing pulse duration.

The considered generalized nonlinear (multi-photon) Compton scattering in short and ultra-short (sub-cycle) laser pulses is a crossing channel to the Breit-Wheeler process and, therefore, reflects the main features of the latter one. We have shown that the fully differential cross section as a function of the frequency of the outgoing photon at fixed production angle is a rapidly oscillating function for short pulses with the duration determined by the number of oscillations $N = 2 \cdots 10$, especially for the flat-top envelope shapes. An experimental study of multi-photon effects in the case of rapidly oscillating cross sections seems to be rather challenging. To overcome the problem of such a staggering we suggest to utilize the partially integrated cross section which seems to be a powerful tool for studying the non-linear (multi-photon) dynamics in the sub-threshold region. We find that these cross sections at selected pulse properties (field intensity, pulse duration) are very sensitive to the pulse shape. In the case of small e.m. field intensities, the cross section may be enhanced by several orders of magnitude as compared to an infinitely long pulse. Such an enhancement is more important for flat-top envelope shapes which generate intensive high-frequency harmonics and play a role of a power amplifier. In the above-threshold region, the partially integrated cross section manifest some "universality" , i.e. an independence of the pulse shape structure, where results for FPA and IPA are close to each other. Note that such a "universality" does not appear in fully differential cross section, where one can find rapidly oscillating cross section as a function of ω', especially for the flat-top envelope shape. At high field intensity, the central part of envelopes becomes dominant and the integrated cross sections coincide with that for infinitely long pulses. It provides a rationale for the use of simple analytical expressions of IPA for Monte Carlo transport approaches. Finally, we have shown that the effect of the carrier phase is important and might be seen clearly in sub-cycle pulses. Similarly to the Breit-Wheeler process, we predict a definite alignment of the differential cross section and anisotropy in the $x-y$ plane along the angle equal to the carrier phase.

Our considerations are focused on circularly polarized photon beams. However, we expect that qualitatively, in the case of a linearly polarized pulse, our main results, i.e. the sensitivity of the production probability of pair production and partially integrated cross section of the Compton scattering to the sub-threshold multi-photon interactions and to the pulse

structure, would be similar. The main difference is expected for the anisotropies since the momentum of the outgoing electron will be correlated with the direction of pulse polarization.

Our considerations are devoted essentially to the elementary processes in optical laser beams. With the availability of X ray beams (XFELs cf.[LCLS, SACLA, European XFEL, Swiss XFEL, ...]) already now or in near future a further field of interesting phenomena is entered, where the here presented theory also applies.

Acknowledgments

The authors acknowledge fruitful discussions with D. Seipt, T. Nousch, T. Shibata, R. Sauerbrey and T. E. Cowan.

Appendix

Production probability at large values of ξ

The total probability W in the limit of large ξ and and small ξ/ζ, was evaluated by Narozhny and Ritus [15] and summarized by Ritus [17] in compact form. Below, for completeness and easy reference, we recall some details of Ritus's evaluation making an expansion for an arbitrary value of ξ/ζ, applying it for the case of the finite pulse (cf. Sect. 3. 5).

In IPA, the total probability is represented as an infinite sum of partial harmonics [17]

$$W = \frac{1}{4}\alpha M_e \zeta \sum_{n=n_0}^{\infty} \int_1^{u_n} \frac{du}{u^{3/2}\sqrt{u-1}} \{2J_n^2(z) + \xi^2(2u-1)\left(J_{n+1}^2(z) + J_{n-1}^2(z) - 2J_n^2(z)\right)\} , \tag{92}$$

where $n_0 \equiv n_{\min} = \zeta(1+\xi^2)$, $u_n = n/n_0$, and $J_n(z)$ is the Bessel function of the first kind (cylindrical harmonics). Using the identities

$$2\,\frac{n}{z}\,J_n(z) = J_{n-1}(z) + J_{n+1}(z), \;\; 2\,J'_n(z) = J_{n-1}(z) - J_{n+1}(z) , \tag{93}$$

the total probability takes the following form

$$W = \frac{1}{2}\alpha M_e \zeta^{1/2} \sum_{n_0}^{\infty} \int_1^{u_n} \frac{du}{u^{3/2}\sqrt{u-1}} \left(J_n^2(z) + \xi^2(2u-1)\left((\frac{n^2}{z^2}-1)J_n^2(z) + J'^2_n(z)\right)\right) . \tag{94}$$

At large $\xi \gg 1$, $\zeta \gg 1$, n, $z \gg 1$ and $n > z$ one can replace the sum over integer n by an integral over dn, replacing, for convenience, integer n to continues l with $l_{\min} \equiv l_0 = \zeta(1+\xi^2)$. Using Watson's asymptotic expression for the Bessel functions one finds

$$J_l\left(\frac{l}{\cosh\alpha}\right) = \frac{1}{\sqrt{2\pi l \tanh\alpha}} e^{-l(\alpha-\tanh\alpha)} + \mathcal{O}\left(\frac{1}{\xi}\right) \tag{95}$$

with $\cosh\alpha = l/z$. If l is large the first term represents a good approximation irrespectively whether ξ/ζ is small or large [51]. The corresponding derivative reads

$$J_l'(z) \simeq \sinh\alpha\, J_l(z)\, \left(1 + \frac{1}{2l\sinh^2\alpha\tanh\alpha}\right) . \tag{96}$$

Consider first the case of small $\xi/\zeta \ll 1$, when the second term in (96) can be neglected. Then, the total probability becomes

$$W = \frac{e^2 M_e \zeta^{1/2}}{8\pi^2} \int\limits_{l_0}^{\infty} dl \int\limits_{1}^{u_l} \frac{du}{u^{3/2}\sqrt{u-1}} \frac{1 + 2\xi^2(2u-1)\sinh^2\alpha}{l\,\tanh\alpha}\, \mathrm{e}^{f(u,l)} , \tag{97}$$

where $u_l = l/l_0$ and $\hat{f}(u,l) = -2l(\alpha - \tanh(\alpha))$ with

$$\tanh^2(\alpha) = \frac{1 + \xi^2\left(1 - \frac{2u}{u_l}\right)^2}{1+\xi^2} . \tag{98}$$

To avoid a notational confusion with respect to the standard variable α, we replace below the fine structure constant by $e^2/4\pi$.

The two-dimensional integral is evaluated using the saddle point approximation since the function $\hat{f}(u,l)$ has a sharp minimum at the point $u = \bar{u}$ defined by the equation $\hat{f}_u'(u=\bar{u}) = 0$. That allows (i) to expand it into a Taylor series

$$f(u,l) \simeq \hat{f}(\bar{u},l) + \frac{1}{2}\hat{f}_u{}''(\bar{u},l)(u-\bar{u})^2 , \tag{99}$$

and (ii) to take the rest (smooth) part of the integrand in Eq. (97) at the point $u = \bar{u}$ yielding

$$W = \frac{e^2 M_e \zeta^{1/2}}{16\pi^2} \int\limits_{l_0}^{\infty} dl\, \mathcal{A}_0(\bar{u},l) \mathrm{e}^{\hat{f}(\bar{u},l)} \int\limits_{1}^{u_l} \frac{du}{\sqrt{u-1}}\, \mathrm{e}^{\frac{1}{2}\hat{f}''(\bar{u},l)(u-\bar{u})^2} , \tag{100}$$

with

$$\mathcal{A}_0(u,l) = \frac{1 + 2\xi^2(2u-1)\sinh^2\alpha}{u^{3/2} l \tanh\alpha} . \tag{101}$$

The explicit expression

$$\hat{f}'_u(u,l) = \frac{4l_0 \sinh^2\alpha}{\tanh\alpha} \frac{\xi^2}{1+\xi^2}\left(1 - \frac{2u}{u_l}\right) \tag{102}$$

leads to the solution

$$\bar{u} = \frac{u_l}{2} = \frac{l}{2l_0}\ , \tag{103}$$

which results in the following equalities

$$\begin{aligned} &\tanh\bar{\alpha} \equiv \tanh\alpha(\bar{u}) = \frac{2}{\sqrt{1+\xi^2}},\ \sinh\bar{\alpha} = \frac{1}{\xi},\ \ \hat{f''}_u(\bar{u},l) = -\frac{8l_0^2}{l\sqrt{1+\xi^2}} \\ &\mathcal{A}_0 = \frac{1+2(2\bar{u}-1)}{\bar{u}^{3/2}l}\sqrt{1+\xi^2},\ \ \hat{f}(\bar{u},l) = -2l(\bar{\alpha} - \tanh\bar{\alpha})\ . \end{aligned} \tag{104}$$

Using the substitutions $u = t+1$, $a = 2(\bar{\alpha} - \tanh\bar{\alpha})$, and $A = -\frac{1}{2}\hat{f}''(\bar{u},l)$ one can rewrite Eq. (100) as

$$W = \frac{e^2 M_e \zeta^{1/2}}{16\pi^2} \int\limits_{l_0}^{\infty} dl\, \mathcal{A}_0(\bar{u},l) \mathrm{e}^{-al - A(1-\bar{u})^2} \int\limits_0^{\infty} dt\, t^{\nu-1} \mathrm{e}^{-\beta t^2 - \gamma t}\ , \tag{105}$$

with $\nu = 1/2$, $\beta = A$, and $\gamma = 2A(1-\bar{u})$. The integral over dt is expressed via the parabolic cylinder function $D_{-\nu}$

$$\int\limits_0^{\infty} dt\, t^{\nu-1}\mathrm{e}^{-\beta t^2 - \gamma t} = \left(\frac{1}{2\beta}\right)^{\nu/2} \Gamma(\nu) \exp[\frac{\gamma^2}{8\beta}]\ D_{-\nu}\left(\frac{\gamma}{\sqrt{2\beta}}\right)\ , \tag{106}$$

which results in

$$W = \frac{e^2 M_e \zeta^{1/2}}{16\pi^{3/2}} \int\limits_{l_0}^{\infty} dl\ \left(\frac{1}{2A}\right)^{\frac{1}{4}} \mathcal{A}_0(\bar{u},l) \mathrm{e}^{-al - \frac{A}{2}(1-\bar{u})^2} D_{-\frac{1}{2}}(y) \tag{107}$$

with $y = \sqrt{2A}(1-\bar{u})$. The main contribution to this integral comes from the region $\bar{u} \sim 1$ ($l \sim \bar{l} = 2l_0$) and, therefore, one can use the substitution

$$\int\limits_{l_0}^{\infty} dl = -\frac{2l_0}{\sqrt{2A}} \int\limits_{\sqrt{A/2}}^{-\infty} dy \approx \frac{2l_0}{\sqrt{2A}} \int\limits_{-\infty}^{\infty} dy\ , \tag{108}$$

which results in

$$W = \frac{e^2 M_e \zeta^{1/2}}{16\pi^{3/2}} \left(\frac{1}{2A}\right)^{\frac{1}{4}} \frac{2l_0}{\sqrt{2A}} \mathcal{A}_0(\bar{u},\bar{l}) \mathrm{e}^{-2l_0 a} \int\limits_{-\infty}^{\infty} dy\, \mathrm{e}^{Zy - y^2/4} D_{-\frac{1}{2}}(y) \tag{109}$$

with $Z = 2l_0 a/\sqrt{2A}$. Using the identity

$$\int\limits_{-\infty}^{\infty} dy\, \mathrm{e}^{Zy-y^2/4} D_{-\frac{1}{2}}(y) = \sqrt{\frac{2\pi}{Z}}\, \mathrm{e}^{Z^2/2} \ , \tag{110}$$

one can rewrite the production probability as

$$W = \frac{e^2 M_e \zeta^{1/2}}{16\pi} \sqrt{\frac{2l_0}{aA}}\, \mathcal{A}_0(\bar{u}, \bar{l}) \exp[-2l_0 a + \frac{l_0^2 a^2}{A}] \ . \tag{111}$$

In order to reproduce the Ritus result [17] in terms of the kinematic factor ζ and the field intensity ξ one has to use the identity $l_0 = \zeta(1+\xi^2)$ and to represent $a(\bar{\alpha})$ as a series for small values $1/\xi$ utilizing the expansions

$$\begin{aligned} \bar{\alpha} \ &= \ \mathrm{arsinh}\frac{1}{\xi} \simeq \frac{1}{\xi} - \frac{1}{6\xi^3} + \frac{3}{40\xi^5} \ , \\ \tanh\bar{\alpha} \ &= \ \frac{1}{\sqrt{1+\xi^2}} \simeq \frac{1}{\xi} - \frac{1}{2\xi^3} + \frac{3}{8\xi^5}, \ \mathcal{A}_0 = \frac{3}{2\zeta\xi} \ , \end{aligned} \tag{112}$$

which leads to (48) with $d = 1$. Inclusion of the second term in (96) modifies eventually $\mathcal{A}_0$ as

$$\mathcal{A}_0 = \frac{3}{2\zeta\xi}\left(1 + \frac{\xi}{6\zeta}\left(1 + \frac{\xi}{8\zeta}\right)\right) \tag{113}$$

yielding the result displayed in (48) which generalizes the Ritus result for arbitrary values of ξ/ζ. We emphasize that, in the strong field regime, IPA is representative (with taking into account the pre-exponential factor $d(\xi/\zeta)$ in (48)) since, as stressed above, pulse shape and pulse duration effects are sub leading.

---

[1] *Mourou G. A, Tajima T, and Bulanov S. V.* Optics in the relativistic regime // Rev. Mod. Phys. 2006. V. 78. P 309-371.

[2] *Di Piazza A., Müller C, Hatsagortsyan K. Z., and Keitel C. H.* Extremely high-intensity laser interactions with fundamental quantum systems // Rev. Mod. Phys. 2012. V. 84. P 1177-1228.

[3] *Yanovsky V., Rousseau P., Planchon T, Matsuoka T, Maksimchuk A., Nees J., Cheriaux G., Mourou G., Krushelnick K.* Ultra-high intensity 300-TW laser at 0.1 Hz repetition rate // Optics Express 2008. V. 16. P. 2109-2114.

[4] `http://www.clf.stfc.ac.uk/CLF/.`

[5] http://www.eli-beams.eu.

[6] http://www.hiper-laser.org.

[7] https://www.ipfran.ru/english/science/las_phys.html.

[8] *Cavalieri A. L., Goulielmakis1 E, Horvath B., Helml W., Schultze M., Fiess M., Pervak V., Veisz L., V S Yakovlev S. V., Uiberacker M., Apolonski A., Krausz F., and R Kienberger R.* Intense 1.5-cycle near infrared laser waveforms and their use for the generation of ultra-broadband soft-x-ray harmonic continua // New J. Phys. 2007. V. 9. P. 242.

[9] *Major Z, Klingebiel S., Krobol C, Ahmad I., Wandt C., Trushin S. A., Krausz. F., and Karsch S.* Status of the Petawatt Field Synthesizer pump-seed synchronization measurements // AIP Conference Proceedings. 2010. V 1228. P. 117-122.

[10] *Mackenroth F. and Di Piazza A.* Nonlinear Compton scattering in ultra-short laser pulses // Phys. Rev. A. 2011. V. 83, P. 032106.

[11] *Feng F., Gilbertson S., Mashiko H., Wang He, Khan S. D., Chini M., Wu Yi, Zhao K., and Chang Z.* Generation of Isolated Attosecond Pulses with 20 to 28 Femtosecond Lasers // Phys. Rev. Lett. 2009. V. 103, P. 183901.

[12] *Krausz F., and Ivanov M.* Attosecond physics // Rev. Mod. Phys. 2009. V. 81. P.163-234.

[13] *Reiss H. R.* Absorbtion of Light by Light // J. Math. Phys. 1962. V. 3, P. 59-67.

[14] *Reiss H. R.* Production of electron pairs from a zero-mass state // Phys. Rev. Lett. 1971. V. 26, P. 1072-1075.

[15] *Nikishov A. I. and Ritus V. I.* Quantum processes in field of a plane electromagnetic wave and a constant field // Sov. Phys. JETP. 1964. V. 19, P. 529-541.

[16] *Narozhny N. V., Nikishov A. I., and Ritus V. I.* Quantum processes in field of a circularly polarized electromagnetic wave // Sov. Phys. JETP. 1965. V. 20, 622-629.

[17] *Ritus V.I.* Quantum effects in the interaction of elementary particles with an intensive electromagnetic field. // J. Sov. Laser Res. (United States). 1985. V. 6:5, P. 497-617.

[18] *Boca M. and V. Florescu V.* Nonlinear Compton scattering with a laser pulse // Phys. Rev. A. 2009. V. 80 P. 053403.

[19] *Heinzl T., Seipt D., and Kämpfer B.* Beam-Shape Effects in Nonlinear Compton and Thomson Scattering // Phys. Rev. A. 2010. V. 81. P. 022125.

[20] *Seipt D., and Kämpfer B.* Non-Linear Compton Scattering of Ultrashort and Ultraintense Laser Pulses // Phys. Rev. A. 2011. V. 83, P. 022101.

[21] *Dinu V., Heinzl T., and Ilderton A.* Infra-Red Divergences in Plane Wave Backgrounds // Phys. Rev. D. 2012. V. 86, P. 085037.

[22] *Seipt D., and Kämpfer B.* Two-photon Compton process in pulsed intense laser fields // Phys. Rev. D. 2012. V. 85. P. 101701.

[23] *Krajewska K. and J. Z. Kaminski J. Z.* Compton Process in Intense Short Laser Pulses // Phys. Rev. A. 2012, V. 85. P. 062102-1-11.

[24] *Titov A. I., Kmpfer B., Shibata T., Hosaka A., and Takabe H.* Laser pulse-shape dependence of Compton scattering // Eur. Phys. J. D. 2014. V. 68. P. 299.

[25] *Titov A. I., Takabe H., Kmpfer B., Hosaka A.* Enhanced subthreshold electron-positron production in short laser pulses // Phys. Rev. Lett. 2012. V. 108, P. 240406.

[26] *Titov A. I., Kmpfer B., Takabe H., and Hosaka A.,* Breit-Wheeler process in very short electromagnetic pulses // Phys. Rev. A. 2013. V. 87, P. 042106.

[27] *Nousch T., Seipt D., Kämpfer B., and Titov A. I.* Pair production in short laser pulses near threshold // Phys. Lett. B. 2012. V. 715. P. 246-250.

[28] *Krajewska K. and J. Z. Kaminski J. Z.* Breit-Wheeler Process in Intense Short Laser Pulses // Phys. Rev. A. 2012. V. 86, P. 052104.

[29] *Villalba-Chavez S. and Müller C.* Photo-production of scalar particles in the field of a circularly polarized laser beam // Phys. Lett. B. 2013. V. 718, P. 992-997.

[30] *Fedotov A.M., Narozhny N. B., Mourou G., and Korn G.* Limitations on the attainable intensity of high power lasers // Phys. Rev. Lett. 2010. V. 105. P. 080402.

[31] *Elkina N. V., Fedotov A. M., Kostyukov I. Y., Legkov M. V. , Narozhny N. B., Nerush E. N. , and Ruhl H.* QED cascades induced by circularly polarized laser fields // Phys. Rev. ST Accel. Beams. 2011. V. 14. P. 054401.

[32] *Ilderton A., Johansson P., and Marklund M.* Pair annihilation in laser pulses: Optical vs. XFEL regimes // Phys. Rev. A. 2011. V. 84. P. 032119.

[33] *Hu H., Müller C., and Keitel C. H.* Complete QED theory of multiphoton trident pair production in strong laser fields // Phys. Rev. Lett. 2010. V. 105. P. 080401.

[34] *Ilderton A.* Trident pair production in strong laser pulses // Phys. Rev. Lett. 2011. V. 106, P. 020404.

[35] *Kirk J. G., Bell A. R., and Arka I.* Pair production in counter-propagating laser beams // Plasma Phys. Control. Fusion. 2009. V. 51. P. 085008.

[36] *Bulanov S. V., Esirkepov T. Zh., Hayashi Y., Kando M., Kiriyama H., Koga J. K., Kondo K., Kotaki H., Pirozhkov A.S., Bulanov S.S., Zhidkov A.G., Chen P., Neely D., Kato Y., Narozhny N. B., Korn G.* On the design of experiments for the study of extreme field limits in the interaction of laser with ultrarelativistic electron beam // Nucl. Instrum. Meth. A. 2011. V. 660, P. 31-42.

[37] *Ruffini R., Vereshchagin G., and Xue S-Sh.* Electron-positron pairs in physics and astrophysics: From heavy nuclei to black holes // Phys. Rept. 2010. V. 487. P. 1-140.

[38] *Breit G. and Wheeler J. A.* Collision of two light quanta // Phys. Rev. 1934. V. 46. P. 1087-1091.

[39] *Blaschke D. B., Kämpfer B., Schmidt S. M., Panferov A. D., Prozorkevich A. V., and Smolyansky S. A.* Properties of the electron-positron plasma created from vacuum in a strong laser field I. Quasiparticle excitations // Phys. Rev. D. 2013. V. 88. P. 045017.

[40] *Schwinger J.S.* On gauge invariance and vacuum polarization // Phys. Rev. V. 82. 1951. P. 664-679.

[41] *Dunne G. V., Gies H., and Schützhold R.* Catalysis of Schwinger Vacuum Pair Production // Phys. Rev. D. 2009. V. 80, 111301.

[42] *Hebenstreit F., Alkofer R., Gies H.* Particle self-bunching in the Schwinger effect in spacetime-dependent electric fields // Phys. Rev. Lett. 2011. V. 107, P. 180403.

[43] *Mackenroth F., Di Piazza A., and Keitel C. H.* Determining the carrier-envelope phase of intense few-cycle laser pulses // Phys. Rev. Lett. 2010. V. 105, P. 063903.

[44] *Hebenstreit F., Alkofer R, Dunne G. V., and Gies H.* Momentum signatures for Schwinger pair production in short laser pulses with a subcycle structure // Phys. Rev. Lett. 2009. V. 102, P. 150404.

[45] *Narozhnyi N.B. and Fofanov M. S.* Photon emission by an electron in a collision with a short focused laser pulse // J. Exp.Theor. Phys. 1996. V. 83. P. 14-23.

[46] *Heinzl T. and Ilderton A.* A Lorentz and gauge invariant measure of laser intensity // Opt. Commun. 2009. V. 282, P. 1879-1883.

[47] *Burke D. L. et al.*(*Collaboration: SLAC E-144 Experiment*), Positron production in multiphoton light by light scattering // Phys. Rev. Lett. 1997. V. 79, P. 1626.!-1-4.

[48] *Grypeos M. E., Koutroulos C., Lukyanov V. K., and A. V. Shebeko A. V.* Properties of Fermi and symmetrized Fermi functions and applications in nuclear physics // Phys. Part. Nucl.

2001 V. 32, P. 779-812.

[49] *Volkov D. M.* Uber eine Klasse von Losungen der Diracschen Gleichung // Z. Phys. 1935. V. 94, P. 250-260.

[50] *Berestetskii V. B., Lifshitz E. M., and Pitaevskii L. P.* Quantum Electrodynamics. 2nd ed., (Course of theoretical physics; vol. 4.) 1982. Oxford, New York, Pergamon Press Ltd.

[51] *Watson G. N.* A Treatise of the Theory of Bessel Functions (The University Press, Cambridge, 1944), 2nd ed.

[52] *Seipt D. and Kämpfer B.* Laser-assisted Compton scattering of x-ray photons // Phys. Rev. A. 2014. V 89. 023433.

[53] *Jochmann A. Irman A., Bussmann M., Couperus J. P., Cowan T.E., Debus A.D., Kuntzsch M., Ledingham K. W. D., Lehnert U., Sauerbrey R., Schlenvoigt H. P., Seipt D., Sthlker Th., Thorn D. B., Trotsenko S., Wagner A., and Schramm U.* High resolution energy-angle correlation measurement of hard X rays from laser-Thomson backscattering // Phys. Rev. Lett. 2013. V. 111. P. 114803.

[54] *Seipt D. and Kämpfer B.* Asymmetries of azimuthal photon distributions in non-linear Compton scattering in ultra-short intense laser pulses // Phys. Rev. A. 2013. V. 88. P. 012127.